

CHALMERS



Experimental measurements of the Jeffery orbits of microrods in microchannels

MSc Thesis in Complex Adaptive Systems

Staffan Ankardal

Department of Applied Physics
CHALMERS UNIVERSITY OF TECHNOLOGY
Gothenburg, Sweden 2013
MSc Thesis 2013:1

Abstract

Orientational motion of axisymmetrical particles in shear flow is important in a number of scientific fields. It was first studied by Jeffery, who showed that an axissymmetrical particle in shear flow will follow one of infinitely many periodic orbits depending on the initial condition of the particle. Later studies by Yarin suggested that asymmetric particles may follow periodic, quasi-periodic, or chaotic orbits depending only on the initial conditions. This thesis attempts to experimentally verify Yarin's predictions for the equations of motion, using glass particles in a reversible Stokes' flow in a microfluidic PDMS channel. An optical tweezer is used to control the initial conditions . An automatic tracking of the particles was developed, and a number of improvements were made compared to previous experiments by Einarsson et al[1]. We study the effects of asymmetry on the particles, and the transition from periodic to quasi-periodic orbits for different initial conditions of particles, and for different degrees of asymmetry. Some measurements show good agreement with theoretical prediction, but there are frequent unexplained behaviours when the flow is reversed. Measurements were made in collaboration with Alexander Laas [2].

Acknowledgements

I hereby wish to thank my supervisors Bernhard Mehlig and Dag Hanstorp for helping me through this journey. I want to thank girlfriend Callie Gibbons for supporting me through the work on this thesis and Alexander Laas for being a tireless and understanding co-worker. I want to thank all the contributors to the wealth of open source software which I have used to create everything from most of the software to more of the figures and of course this very report.

Staffan Ankardal, Göteborg Sweden March 10, 2014

Contents

1	Introduction	1
1.1	Introduction	1
1.1.1	Background	1
2	Theory	4
2.1	Fluid dynamics	4
2.1.1	Reynolds Number	4
2.1.2	Stokes drag and Stokes' law	6
2.2	Euler angles and coordinate system	7
2.2.1	Triaxial particles	9
2.3	Jeffery orbits	9
2.3.1	Winding number	13
3	Method	16
I	Improvements of Experimental Setup	17
3.1	Experimental Setup	18
3.1.1	List of equipment	22

3.2	Problems and Improvements	22
3.2.1	Particles and channel	23
3.3	Automated tracking	26
3.3.1	Acquiring the image	26
3.3.2	Reducing noise	26
3.3.3	Contour detection and selection	27
3.3.4	Adjusting the camera velocity	28
3.3.5	Time Considerations	29
3.4	Summary of improvements	29
II	Data analysis and results	31
4	Data Analysis	32
4.1	Particle identification	32
4.2	Estimation of orientation	33
4.3	Width compensation	34
4.4	Removing tracking errors	35
4.5	Estimating the winding numbers	36
4.6	Matching data to theoretical orbits	38
5	Results	40
5.1	Measurements	42
5.1.1	Measurements of Particle A	42
5.1.2	Measurements of Particle B	45
5.2	Diagnostic plots	48
5.2.1	Reversals	51
5.3	Match to theoretical orbits	53
5.3.1	Particle A	53
5.3.2	Particle B	54

6 Discussion	57
6.1 Sinking	58
6.2 Reversals	58
6.2.1 The speed of the particle	59
6.3 Winding number matching	60
6.4 Unexplained behaviours	60
6.5 Width compensation	61
6.6 Goodness of fit	61
7 Conclusion	65

1

Introduction

1.1 Introduction

My goal in this thesis is to study and better understand the dynamics of ellipsoidal particles in shear flows. The thesis is a continuation of two previous MSc theses[3, 4]. The methodology is to experimentally measure the orientational dynamics of micrometer length glass particles in a shear flow, then comparing the results to those of theoretical models. In the first part of the thesis, I describe the improvements that were made to the experimental setup, most importantly an automated tracking system. In the second part of the thesis, the measurements and their analysis is discussed. But before discussing either of these subjects more in depth some background and theory is needed.

1.1.1 Background

Understanding the orientational dynamics of particles in flow might appear somewhat esoteric to someone unfamiliar with the field, but there are a number of topics where it is very useful. In medical applications understanding the dynamics of ellipsoidal particles such as bacteria can be relevant to a detailed understanding of their interactions with cells and other bodies. This is discussed by

1.1. INTRODUCTION

Tolga *et al* [5]. In geology the rotation of mineral grains approximated by ellipsoids are used in models of rock formation in an article by Cañón-Tapia and M.J. Chávez-Álvarez [6].

One of the most influential papers in the study of particle dynamics in flow was by Einstein in 1905 [7]. He showed how much suspended spherical particles increase the viscosity of a fluid. Jeffery in his 1922 paper [8] extended these results to ellipsoidal particles and derived equations for the orientational dynamics of axisymmetric particles, in other words how the particles would rotate as a function of time. For systems where inertial effects could be disregarded the motion was found to be periodic and depending only on the initial condition of the particle.

Investigation of triaxial particles was started by Gierszewski & Chaffey [9] and was continued by Hinch & Leal [10] and more recently by Yarin *et al* [11]. The dynamics Jeffery had found for axisymmetric particles were periodic, but it was shown by Hinch & Leal that for triaxial particles some orbits would be doubly periodic, in other words following two separate independent periods. This behaviour will in this thesis be referred to as *quasi-periodic*.

Yarin *et al* used numerical simulations to generate a surface of section [12] for ellipsoidal particles with different shapes. They showed that not only were there double periodic or quasi periodic orbits but when the particles were sufficiently different from axisymmetric there would be chaotic orbits. Several other surfaces of section were produced by Johansson [3] using the same method as Yarin. It was shown that even small asymmetries of the order of 1% lead to quasi-periodic motion for some initial conditions.

Attempts to experimentally verify these theoretical results were initially performed by Goldsmith and Mason in 1962 [13] who used flow in a glass pipe to observe the rotation rate for several different particle shapes. They confirmed that the rotation rate matched well with that predicted from Jeffery orbits but they did not study the actual orbits. Since then most experimental research, such that as by Harlen and Koch [14] has focused on how diluted suspensions of particles affect the properties of a liquid. Only tangential efforts such as by Tolga [5] were concerned with the Jeffery orbits. A good summary of both theoretical and experimental results was written by Petrie [15] in 1999.

The first dedicated experiments to measure the actual Jeffery orbits in angular components and verify the orientational dynamics were performed by Einarsson *et al* [1]. Some particle showed

1.1. INTRODUCTION

orbits that could be qualitatively shown to be similar to some Jeffery orbits. These particles also very closely retraced the orbit when reversing the flow implying that no significant amount of noise had disturbed them nor had there been any inertial effects. the vast majority of particles were asymmetric to the degree that their orbits were chaotic or highly quasi-periodic. No particular particle could also be shown to exhibit both quasi periodic and periodic motion. Moreover the width and length of particles varied greatly and could not be measured accurately.

The goal of this thesis is to improve the setup from Johansson[3] and Einarsson *et al* [1] in order experimentally verify the results of Yarin and Hinch, Leal[10, 11]. The aim is to show that the same particle exhibit different types of motion for different initial conditions. Furthermore that different particles may show different motion for the same initial conditions. To this end it is necessary to observe the orientation of a micrometer length particle in a creeping shear flow. The flow is shown to be creeping by demonstrating that the particle dynamics revert as the flow is reversed. The results are compared to theoretical predictions for different initial conditions and asymmetries.

2

Theory

In order to better understand the results and discussions in this thesis basic knowledge of fluid dynamics, image analysis and other fields is needed which will be given in this chapter.

Since the main focus of this thesis is experimental, this chapter will not be entirely thorough. A more inquisitive reader is recommended to read Einarssons licentiate [16] which goes into greater detail on most of the topics covered in this section.

2.1 Fluid dynamics

In order to understand the motivations for, as well as the limitations, and behaviour of the experiment we need to know about a few key concepts in fluid dynamics.

2.1.1 Reynolds Number

The Reynolds number (Re) is a dimensionless number describing the ratio of inertial forces to viscous forces in a flow. Roughly speaking one can think of viscous forces as acting to keep adjacent fluid elements moving in the same direction whereas inertial forces act to prevent any change in the motion of a fluid element. For a flow it defined as [17]

$$\text{Re} = \frac{UL\rho}{\mu} \quad (2.1)$$

where U is the characteristic velocity of the flow, L is the characteristic length, ρ is the density of the fluid and μ is its dynamic viscosity. This is used to estimate the 'regime' of the flow, of which there are two primary types.

1. The laminar regime, where viscous forces dominate over inertial forces
2. The turbulent regime where inertial forces dominate.

A simple visual characterization of the flow types can be seen in figure 2.1.

Flow with $\text{Re} \ll 1$ is referred to as *Stokes flow*. In this regime we can ignore inertial forces completely. This has the implication that not only is the flow guaranteed to be laminar, but it is time reversible. If there are particles in the flow they will also revert perfectly as long as they too have a Reynolds number that is much smaller than 1 [18]. The Reynolds number of a particle is referred to as the particle Reynolds number and is defined as [16]

$$\text{Re}_p = \frac{u_p L \rho}{\mu} \quad (2.2)$$

where u_p is the typical flow speed relative to the particle surface, L is the characteristic size of the particle, ρ is the density of the fluid and μ is the dynamic viscosity of the fluid.

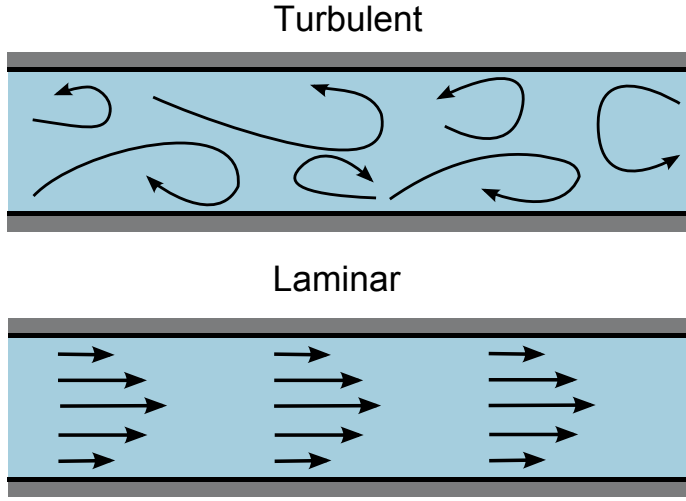


Figure 2.1: This shows the principal difference between laminar and turbulent flow.

2.1.2 Stokes drag and Stokes' law

The drag force F_D exerted by a fluid on a spherical particle for $\text{Re} \ll 1$ is found using Stokes's law [19]

$$F_D = 6\pi\mu Rv, \quad (2.3)$$

where v is the velocity of the sphere relative to the fluid, μ is the dynamic viscosity and R is the radius of the sphere. This can be used to find the terminal velocity of a sphere sinking in a liquid by equating the gravitational force F_G acting on the sphere with the drag force from eq 2.3. F_G is calculated as

$$F_G = \Delta\rho g \cdot \frac{4\pi R^3}{3}, \quad (2.4)$$

where $\Delta\rho$ is the difference in density between the fluid and the sphere and g is the specific gravity. We find that the terminal velocity of a sinking (or floating) sphere is

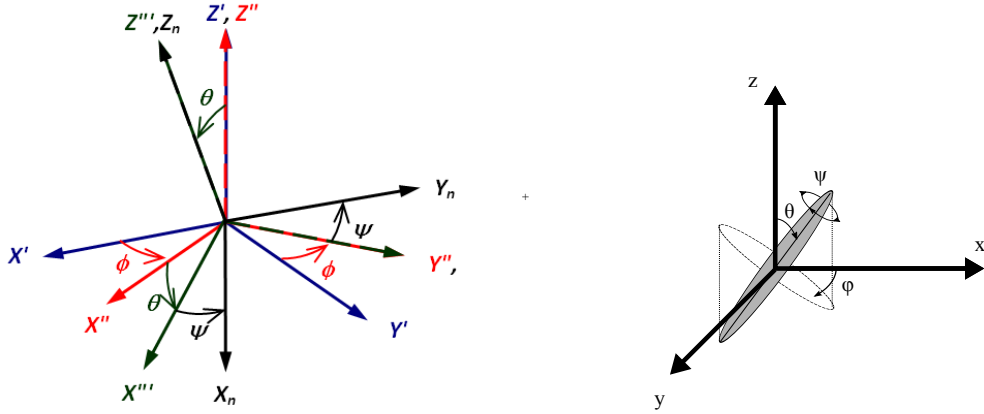
$$v_s = \frac{2}{9} \frac{\Delta\rho}{\mu} g R^2. \quad (2.5)$$

2.2 Euler angles and coordinate system

When describing rotating particles it is common to use the so-called Euler angles $\mathbf{E} = (\phi, \theta, \psi)$. A formal definition is given by Diebel [20] but for the purposes of this thesis we will describe them as a transformation from our stationary coordinate system $\{x,y,z\}$ to the coordinate system attached to our particle $\{x',y',z'\}$. This transformation is performed in three steps by using the intermediate axis T.

- Rotate the x - y plane ϕ radians about the z -axis.
- Denote the shifted x -axis T and rotate the z - y' plane θ radians around the T -axis
- Rotate the x' - y' plane ψ radians around the z' axis.

This is illustrated in figure 2.2a where each prime marks one additional step of rotation to the coordinate system. Figure 2.2b shows the Euler angles for a triaxial particle from a point of view similar to that of the experiment where the x - z plane is the field of view. Note that although ψ has an impact on the particle dynamics, we cannot observe it in our experiment as the particles are too symmetric around that axis, as is shown in section 3.2.1



(a) A general illustration of the Euler angles (b) The Euler angles as used in our experiment

Figure 2.2: Figure (a): The Euler angles illustrated using a series of coordinate rotations. Figure (b): The Euler angles illustrated using an ellipsoid. This alternate visualization shows the angles with a point of view similar to that of the camera in the experiment.

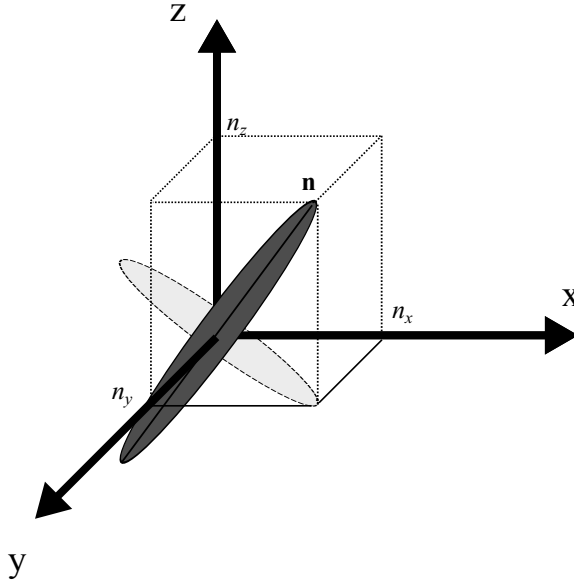


Figure 2.3: The unit vector \mathbf{n} and its components n_x , n_y and n_z . The vector \mathbf{n} is a unit vector, $|\mathbf{n}| = 1$.

The conversion from $\mathbf{E} = (\phi, \theta, \psi)$ to the unit vector $\mathbf{n} = (n_x, n_y, n_z)$ is given by

$$n_x = \sin(\theta) \cos(\psi), \quad (2.6a)$$

$$n_y = \sin(\theta) \sin(\psi), \quad (2.6b)$$

$$n_z = \cos(\theta). \quad (2.6c)$$

2.2.1 Triaxial particles

Triaxial particles have, as the name suggests, three axes which are have distinct lengths, compared to a sphere where all axes have the same length and spheroids that has two axes with distinct lengths. I will in this thesis refer to the lengths of these axes as a_x, a_y, a_z corresponding to their lengths along the (x,y,z) axes when the rotation vector $\mathbf{E} = (0,0,0)$.

When discussing triaxial particles that are close to being axisymmetric of the form $a_x \gg a_y \approx a_z$, convenient to introduce the particle asymmetry ϵ defined as

$$\epsilon = \frac{a_y}{a_z} - 1, \quad (2.7)$$

and the aspect ratio λ given by

$$\lambda = \frac{a_x}{a_y}. \quad (2.8)$$

as used by among others Yarin *et al*[11].

2.3 Jeffery orbits

The Jeffery orbits describe the motion of an ellipsoidal particle in Stokes flow. The orbits for axisymmetric ($a_x = a_z \neq a_y$) ellipsoidal particles were found by Jeffery and reformulated by Yarin *et al* [11] who computed orbits for asymmetric particles. The equations of motion for a triaxial particle in the form of Yarin *et al* is

$$\frac{d\theta}{dt} = (g_2 \sin \psi + g_3 \cos \psi) \sin \theta, \quad (2.9a)$$

$$\frac{d\phi}{dt} = \frac{1}{2} + g_3 \sin \psi - g_2 \cos \psi, \quad (2.9b)$$

$$\frac{d\psi}{dt} = g_1 + (g_2 \cos \psi - g_3 \sin \psi) \cos \theta \quad (2.9c)$$

$$(2.9d)$$

where the functions g_i are defined as

$$g_1 = \frac{a_y^2 - a_z^2}{2(a_y^2 + a_z^2)} \left(-\frac{1}{2}(\cos^2 \theta + 1) \sin 2\phi \sin 2\psi + \cos \theta \cos 2\phi \cos 2\psi \right), \quad (2.10a)$$

$$g_2 = \frac{a_z^2 - a_x^2}{2(a_x^2 + a_z^2)} \left(-\cos \theta \sin 2\phi \sin \psi + \cos 2\phi \cos \psi \right), \quad (2.10b)$$

$$g_3 = \frac{a_x^2 - a_y^2}{2(a_x^2 + a_y^2)} \left(\cos \theta \sin 2\phi \cos \psi + \cos 2\phi \sin \psi \right). \quad (2.10c)$$

where (ϕ, θ, ψ) are the Euler angles seen in figure 2.2a and .

Looking at figure 2.4b we see that n_x and n_y have periodic orbits, we call each one of these periodic changes a flip. The period of flipping T is for an axisymmetric particle [8]

$$T = 2\pi \left(\lambda + \frac{1}{\lambda} \right) \frac{1}{\kappa}, \quad (2.11)$$

where κ is the shear rate.

Solutions to the equations of motions can be found with numerical methods as shown by Yarin [11]. Note that the eq. 2.9 uses the coordinates from Yarin which differ from the ones used in this thesis in the same way as is discusse in Johansson [3]. The time evolution of θ and ψ for different initial conditions can be plotted in a Poincaré map, also known as a Surface-of-Section (S.O.S.) [21]. This plots the ψ and θ coordinates each time $\phi = 0$. The points for every initial condition is bound to a certain region of such a map called the orbit. A few such maps are shown in Figure 2.5

2.3. JEFFERY ORBITS

For a particle with an $\epsilon \in [0.01 - 0.05]$ there are essentially three classes of orbits based on the initial condition θ_0 .

1. **Periodic:** $|\theta_0| \approx 1$ in which there is little variation and the particle is largely periodic with fluctuations too small to measure.
2. **Quasi-periodic sign preserving:** For $|\theta_0| > \theta_b$ the amplitude of $\cos(\theta)$ changes noticeably but does not change sign. θ_b is some breaking point that changes for different ϵ
3. **Quasi-periodic sign changing:** For small $|\theta_0|$ the amplitude of $\cos(\theta)$ will change noticeably and change in sign from positive to negative.

For larger asymmetries $\epsilon > 0.05$ there are chaotic orbits that appear as areas with dots. Chaotic orbits can be seen around the quasi-periodic circular orbits in figure 2.5d where they appear as a 'sea' of dots.

Simulations of these three different types of orbits are illustrated in figure 2.4 both on the S.O.S. as well as the components of \mathbf{n} as a function of time. We can see that while n_x and n_y are periodic, albeit with different amplitudes, the behaviour of n_z is significantly different. For the $n_z \approx 1$ orbit shown in green it is constant on the S.O.S and is simply periodic over time. For the sign preserving quasi-periodic orbit in red it is bent on the S.O.S and we can see in the time series that it is doubly periodic as it peaks with a fixed period but the amplitude of the peaks vary periodically themselves. For the sign changing quasi-periodic orbit in blue n_z changes sign, again with a fixed period.

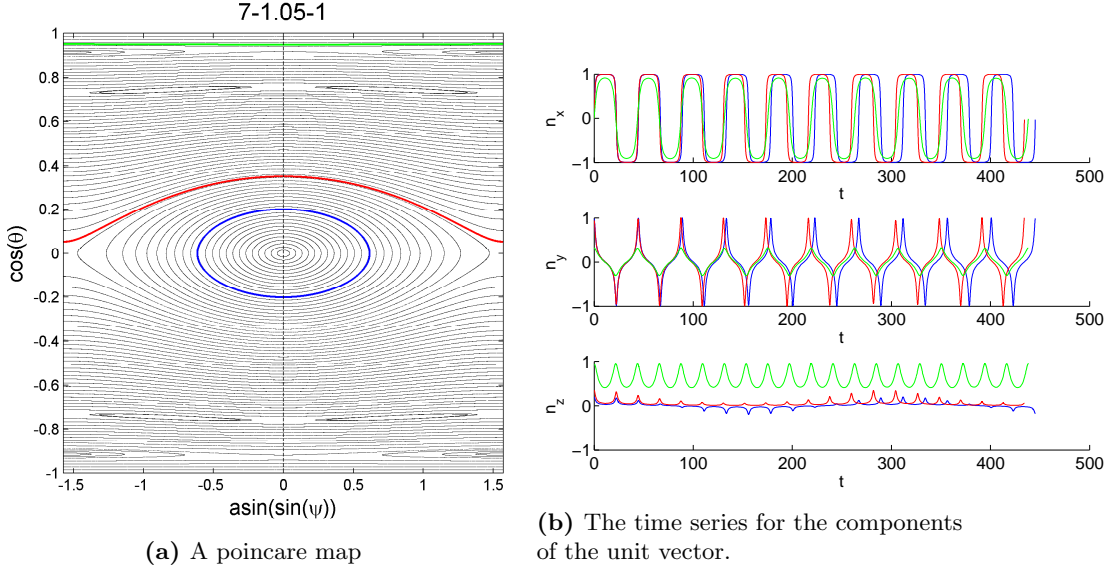


Figure 2.4: A Poincaré map and three different orbits for a simulated particle with $\lambda = 7$ and $\epsilon = 0.05$. The three orbits highlight the three different kinds of motion, the quasi-periodic sign changing orbit in blue, the quasi-periodic sign preserving orbit in red and the periodic orbit in green. We see that while n_x and n_y look qualitatively similar but differ in amplitude for the different orbits, n_z shows three different types of behaviour

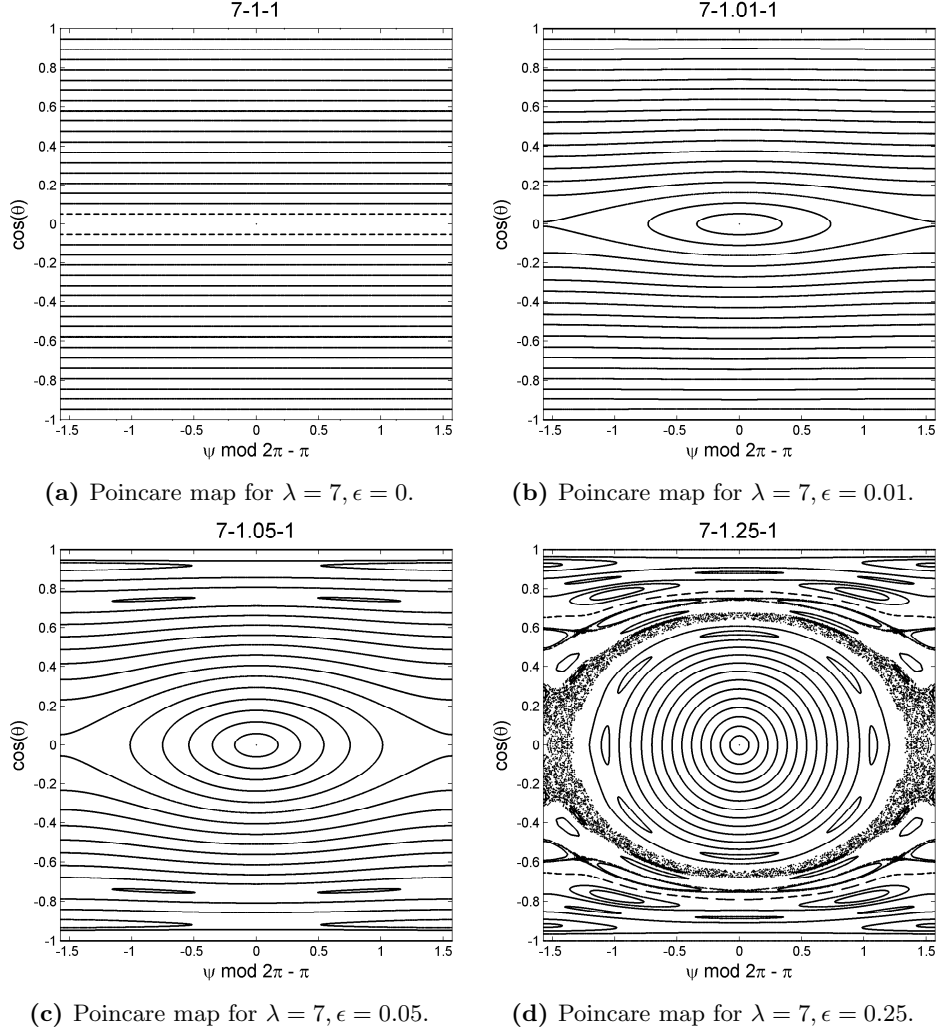


Figure 2.5: Four Poincare maps for different ϵ . Already at $\epsilon = 0.01$ there are noticeably quasi-periodic orbits around the centre at $\cos(\theta) \approx \psi \approx 0$ but it is also a significantly larger region for $\epsilon = 0.05$. For $\epsilon = 0.25$ we can see chaotic orbits surrounding the circular orbits in the centre that appear as a 'sea' of dots. Note that some wavelike pattern can appear to exist in the figure 2.5b and 2.5b, this is caused by aliasing/compression issues with printing several curved lines close together.

2.3.1 Winding number

The quasi-periodic orbits are also referred to as double-periodic [11]. This to emphasize the fact that the amplitude of the short period θ_2 also varies periodically with period θ_1 . The ratio between

the two periods is referred to as the winding number ω

$$\omega = \frac{\theta_1}{\theta_2}. \quad (2.12)$$

The winding number of the quasi-periodic sign preserving orbit from figure 2.4 is illustrated in Figure 2.6.

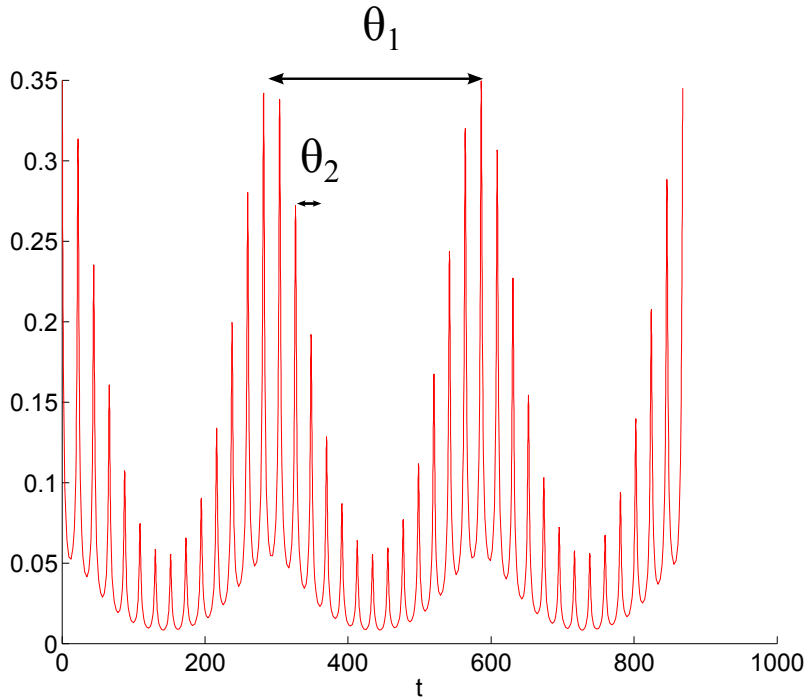


Figure 2.6: The n_z sign preserving quasi-periodic orbit from figure 2.4b over a longer time, highlighting the short period θ_2 which is simply the period of ϕ and the longer period θ_1 . The winding number is defined as the ratio between the longer and shorter periods.

This number is the same for any point along a given orbit on a poincare map but changes for different orbits as well as for different asymmetries. The winding numbers for orbits along $\psi = 0$ for $\epsilon = \{0.01, 0.05, 0.10\}$ can be seen in figure 2.7. This shows us that if we can measure the winding number it allows us to approximate the asymmetry of the particle. This is done by looking at the difference in winding number between a quasi-periodic sign preserving orbit and a sign changing

orbit. This is useful in order to differentiate between particles of different asymmetry, because they can have similar orbits but very distinct winding number.

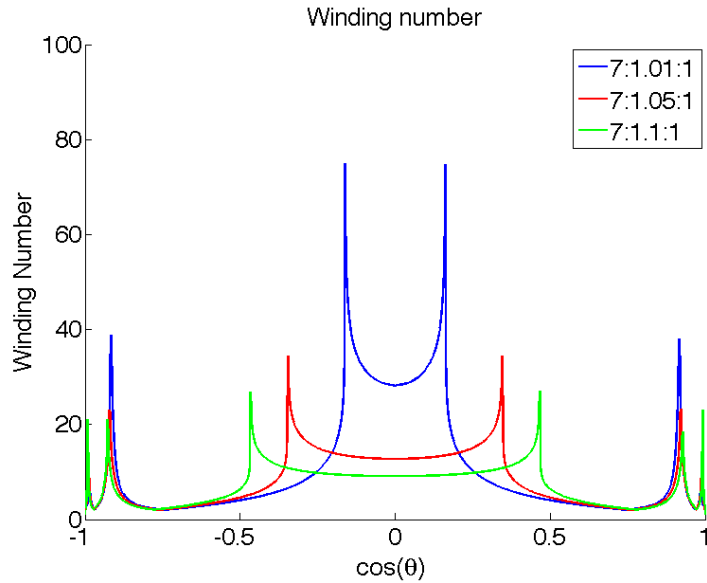


Figure 2.7: The winding number as a function of $\cos(\theta)$ for three different asymmetries. The sharp edge that occurs centered around zero is where the sign changing orbits end and sign preserving orbits begin. We see that a lower asymmetry leads to a sharper difference between the sign changing and the sign preserving orbits.

3

Method

Part I

Improvements of Experimental Setup

3.1 Experimental Setup

The orientational motion of μm sized particles suspended in a liquid was investigated by pumping the liquid through a microfluidic channel using a syringe pump. The channel is placed on a moveable stage on top of a microscope. A particle is tracked by moving the stage to match the center of mass velocity of the particle in the channel and thus keep the particle stationary in the field of view of the microscope. Connected to the microscope is a CCD camera recording the images and these movies are saved on a computer.

When the tracked particle gets within 1 cm of the inlets on the channel the flow is reversed. In order to reduce the sudden impact of the pressure difference the reversals are incremental. At the start of a reversal the infusion/withdrawal rate is reduced by 50% for 10 seconds, then stopped completely for 10 seconds. After this the flow is reverted at 50% of the normal flow rate for another 10 seconds before resuming at full speed.

We refer to the data of a particle along one length of the channel a **stretch** and a series of stretches for a single particle a **measurement**. A sketch of the experimental setup can be seen in figure 3.1, and a photograph of the actual setup in figure 3.2.

Between measurements, optical tweezers constructed by A. Laas were used to change the orientation of the particle. For details on optical tweezers function see the introductory guide from Stanford [22] or Laas thesis [2].

3.1. EXPERIMENTAL SETUP

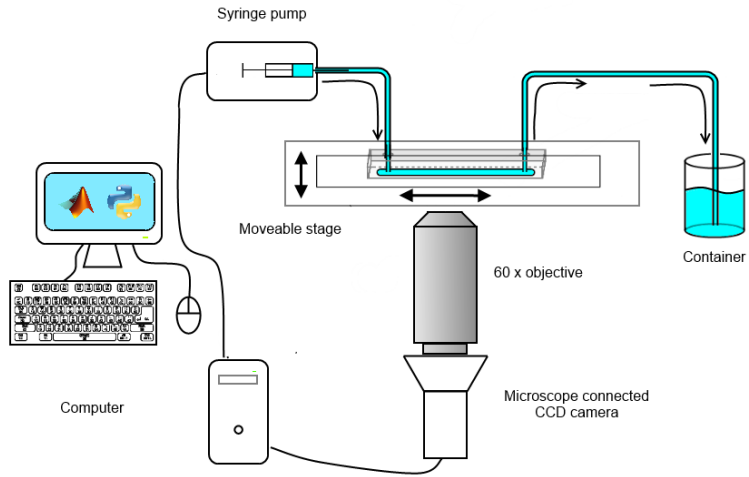


Figure 3.1: Sketch of the set up. The computer controlled stage moves over the microscope. The pump reverses when the tracked particle gets close to the inlets of the channel.

3.1. EXPERIMENTAL SETUP



Figure 3.2: Overview of the set up. The microscope to the left and the syringe pump to the right. In the center is the channel and the outlet container is seen behind it. The CCD camera is mounted on the left side of the microscope and cannot be seen in this picture.

The microfluidic channel is 40 mm long, 2.5 mm wide and approximately 150 μm deep. The channel is made from Polydimethylsiloxane (PDMS) and plasma bonded to a microscope slide. A more detailed description of the process can be found from the Center for Computer Integrated Systems for Microscopy and Manipulation [23]. This material and procedure is chosen so that a channel that gets filled with dirt or breaks can cheaply and easily be replaced. PDMS is also non-reactive and highly transparent. A sketch of the channel can be seen in figure 3.3a, and a photograph of an actual channel in figure 3.3b.

3.1. EXPERIMENTAL SETUP

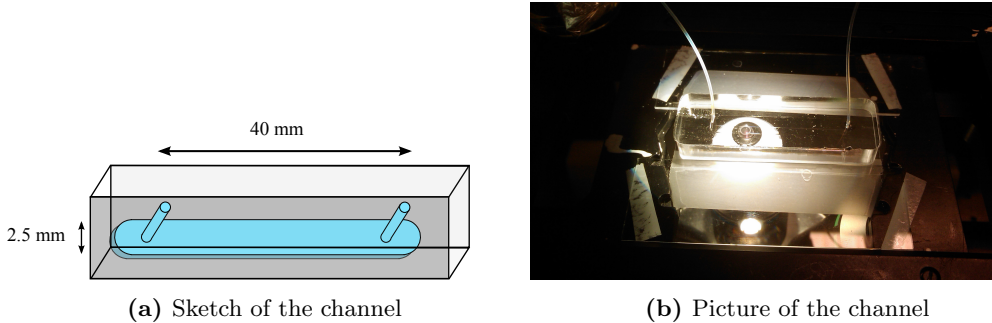


Figure 3.3: A sketch of the channel as well as a picture of the channel as it is set up during a measurement. The channel is only $150\text{ }\mu\text{m}$ deep, but the PDMS surrounding it is around 15 mm to try and prevent the channel from expanding and contracting too much.

In order to find the maximum flow speed of the channel we need to know the flow profile. Using the software employed by Johansson [3] we obtain the flow profile that can be seen in figure 3.4. Integrating the flow profile over the entire surface will give us an effective flow area, essentially how large the channel 'actually' is. Using the flow profile from figure 3.4 we find that the effective flow area is 0.14 mm^2 . With a pump rate of $7.5\text{ }\mu\text{l}/\text{minute}$ we get a maximum velocity of 0.90 mm/s for the liquid.

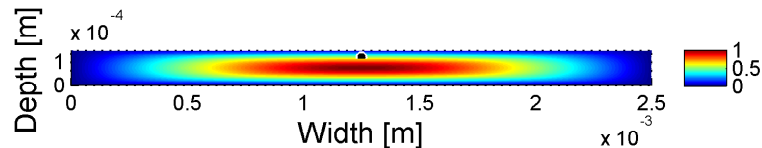


Figure 3.4: The theoretical estimation of the flow profile. Image generated with software from Johansson [3], used with permission.

We need to confirm that the flow is Stokes' flow and thus have no inertial effects. We can calculate the maximum Reynolds number using eq 2.1, the $3\text{ }\mu\text{m}$ length rods, and our maximum flow speed.

$$\text{Re} = \frac{UL\rho}{\mu} \leq \frac{9.0 \cdot 10^{-4} \cdot 3 \cdot 10^{-3} \cdot 2.5}{24 \cdot 10^{-3}} \approx 2.78 \cdot 10^{-6} \ll 1. \quad (3.1)$$

This should satisfy the conditions of validity for the Jeffery equations.

To track the particles the channel is put in a moveable stage on a confocal microscope. The

3.2. PROBLEMS AND IMPROVEMENTS

entire setup can be seen in figure 3.2

3.1.1 List of equipment

The equipment used during the experiment is as follows

- Leica DFC350 FX digital camera
- Nikon Eclipse TE 300 microscope
- Nikon 60x water immersion objective
- Märzhäuser Wetzlar 'LStep-eco' step engine
- CMA 4004 syringe pump
- Ytterbium fiber laser

3.2 Problems and Improvements

As mentioned above this thesis is a continuation of previous work [1, 3, 24]. There were a number of problems that needed to be solved in order to improve the results. They can be summarized as:

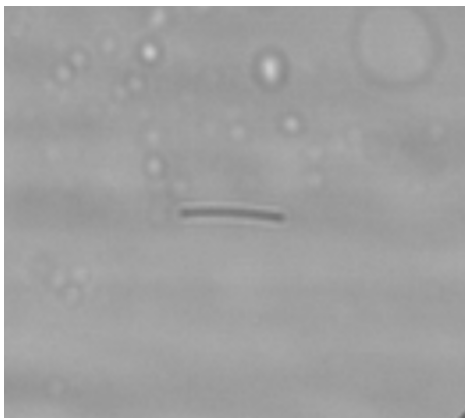
1. Particles

- Very few particles used in previous experiments were sufficiently symmetric to have periodic orbits or even quasi-periodic orbits. Most were visibly bent or uneven, see figure 3.5
- The average aspect ratio of the particles was very high which meant there were very few flips along a stretch.
- The width of the particles was highly irregular and the resolution of the microscope did not allow for accurate measurements of it. This meant it was difficult to accurately estimate the aspect ratio.
- The particles could not be trapped with an optical tweezers due to low transmittance.

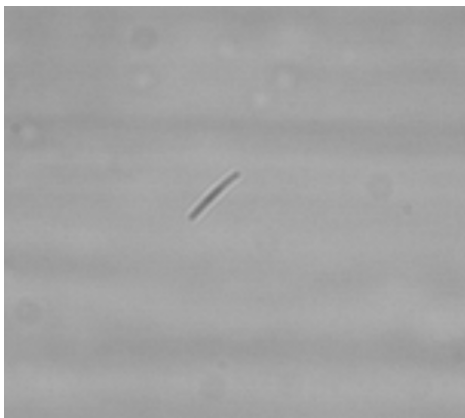
3.2. PROBLEMS AND IMPROVEMENTS

2. The PDMS in the channel was jagged which gave rise to noise unless the focus was in a very narrow band.
3. Manual tracking of particles was time consuming.
4. Bubbles are difficult to avoid when setting up the experiment.

3.2.1 Particles and channel



(a) Particle 13 from July 2012



(b) Particle 22 from July 2012

Figure 3.5: Two typical particles from the previous setup. Note that these are still selected from the total pool of particles for being relatively symmetric and yet are noticeably bent.

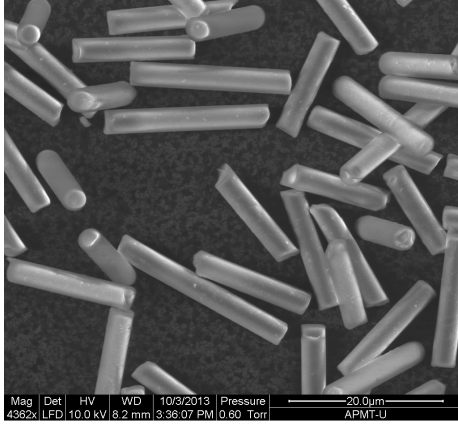
The polymer particles were replaced with glass particles from Nippon Glass, Japan [25].

The new particles are made from LCD spacing rods that are broken into pieces. This means that they are essentially broken cylinders with very homogeneous widths but quite disparate lengths. Two different batches of particles were used, one with a $3\mu m$ diameter and one batch with $5\mu m$ diameter. All the measurements presented in the results section are using the $3\mu m$ width particles. This is primarily as they were more easily controlled with the optical tweezers.

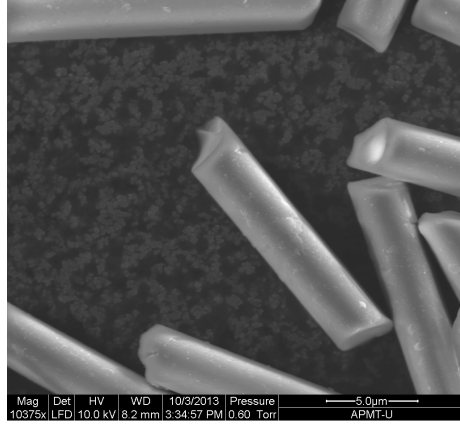
The symmetries of the particles were investigated with help from Stefan Gustafsson by taking images with an ESEM (Environmental Scanning Electron Microscope) shown in Figure 3.6. We see that the particles are uniformly smooth along the sides but have varyingly jagged edges causing different degrees of asymmetry.

3.2. PROBLEMS AND IMPROVEMENTS

Figure 3.7b shows a particle along the main axis and we see that it is almost perfectly circular shape with no discernible asymmetry whereas figure 3.6 show the jagged edge of several particles.

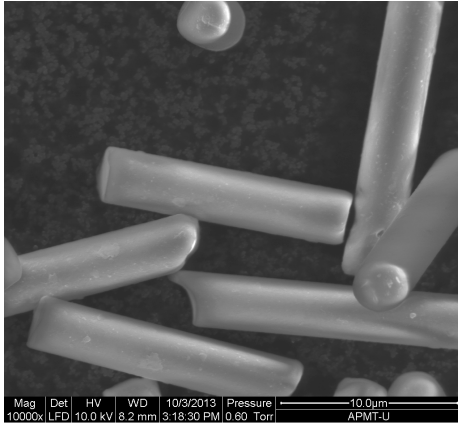


(a) A detailed view
of a number of particles.

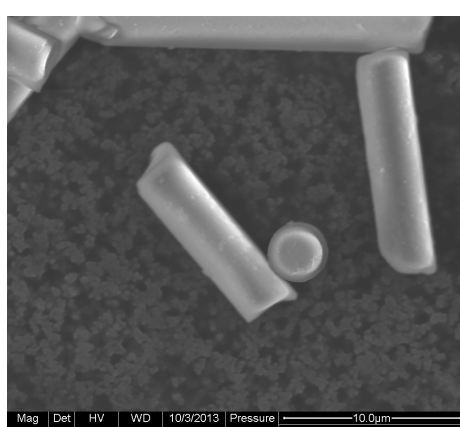


(b) The jagged edge of a particle
in detail.

Figure 3.6: Pictures of the glass particles that were used. Their width is highly uniform and there is a noticeable variance in asymmetry. Some particles show very clearly jagged edges while other appear very smooth. This suggests that they should have quite different ϵ and then exhibit quite different behaviour. Obtained with the help of Stefan Gustafsson



(a) What appears to be a highly
symmetric particle.



(b) A top down view of a particle.

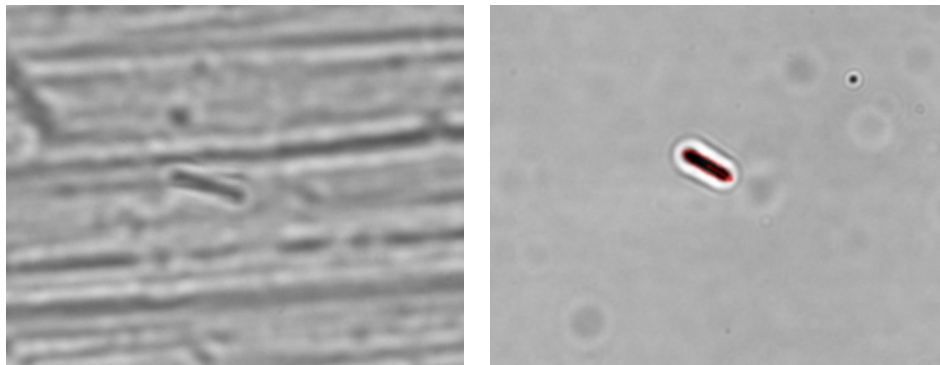
Figure 3.7: Pictures highlighting the roundness of the particles as well as the apparent symmetry of some particles. It should be noted that although there are no apparent rough edges there was no way to rotate a sample so there might very well be asymmetries on the side of the particle that we cannot see. Obtained with the help of Stefan Gustafsson

3.2. PROBLEMS AND IMPROVEMENTS

Figure 3.7b and 3.7a are the same as can be seen in [2] figure 5.2(c) and 5.2(b) respectively.

The particles satisfy the symmetry conditions but are made of glass with a density of approximately 2.57 g/cm^3 at 20°C . This is significantly higher than that of water with a density of 1 g/cm^3 at 20°C and glycerol with a density of 1.5 g/cm^3 . Thus to keep the particles buoyant the water soluble Sodium metatungstate is added to the liquid. Sodium metatungstate dissolved in water has a density of 2.94 g/cm^3 at 20°C when fully saturated. To increase the viscosity of the liquid around 8% glycerol is added and the liquid was measured using a MCR 302 rheometer to have a dynamic viscosity of $24 \cdot 10^{-3} \text{ Pa s}$.

A problem in finding and tracking a particle was that the surface of the PDMS was very uneven and sharp ridges along the length of the channel appear as in figure 3.8a unless the focus was in a relatively narrow depth of the channel.



(a) An unusually severe case of the PDMS edges creating noise. (b) After being polished there is no trace of such ridges.

Figure 3.8: Pictures highlighting the roundness of the particles as well as the apparent symmetry of some particles. It should be noted that although there are no apparent rough edges there was no way to rotate a sample so there might very well be asymmetries on the side of the particle that we cannot see.

This was fixed by polishing the copper mold in which the PDMS channels are formed with a silicate abrasive (Autosol) and emery cloth. This was shown to remove all visible scratches from the mold and thus from the PDMS. As seen in Figure 3.8b no scratches can be detected.

3.3 Automated tracking

One of the most time consuming aspects of making measurements is manually tracking a particle using the movable stage as described in section 3.1. Depending on the flow rate and the number of stretches and measurements desired for a particle it can take up to several hours. Thus one of the primary targets for improvement as discussed by Johansson [3] was automate the camera tracking. This would speed up measurements and allow for a larger data set to be gathered.

Such a tracking was implemented using Python and the external packages `OPENCV`, `NumPy`, `SciPy`, `ImageMagick` and `ctypes`. The goal of the tracking is relatively similar to the tracking described in 4.1 and more in detail in Johansson [3]. The main difference is that the tracking describe in this section moves the actual stage and control the pump in real time whereas Johansson tracking tracks the particle in the movie after manual measurements have been made. This produces some different problems which are detailed below.

3.3.1 Acquiring the image

The first step in tracking a particle is to acquire the image from the microscope in order to identify (and track) the particle. However the Leica DFC350 FX camera only works with the proprietary Leica software which means there is no easy way to get the image straight from the camera in real time. To solve this we use the `ImageGrabber` package in Python to isolate the camera image from the screen by cropping the image aquired. While being a very short program it still takes ca 50 ms per frame. Each frame is stored as a matrix \mathbf{F} with brightness values ranging from 0 to 255.

3.3.2 Reducing noise

In order to reduce noise from the image we first reduce the static noise caused by dirt, scratches and other defects in the microscope and on the camera lens, as shown in figure 4.1a. As the noise is static it is the only thing that will remains if we compute an average image $\bar{\mathbf{F}}$. After taking N images and denote them $\{\mathbf{F}_1, \mathbf{F}_2, \dots, \mathbf{F}_N\}$ the average images $\bar{\mathbf{F}}$ is given by

$$\bar{\mathbf{F}} = \frac{1}{N} \sum_{i=1}^N \mathbf{F}_i. \quad (3.2)$$

An example of such an average image can be seen in figure 4.1b. The static noise is then removed from each frame using eq 3.1 from Johansson [3].

$$\widetilde{\mathbf{F}}_i = \mathbf{F}_i - \bar{\mathbf{F}} + (F_i^* \mathbf{I}) \quad (3.3)$$

where \mathbf{F}_i^* is the average brightness of the frame \mathbf{F}_i , $\widetilde{\mathbf{F}}_i$ is the corrected frame and \mathbf{I} is a matrix of ones. The result can be seen in figure 4.1c.

3.3.3 Contour detection and selection

The edges of the captured image are detected using the Canny edge detector from the OpenCV package. The canny edge detector takes two thresholds for finding edges, τ_1 and τ_2 with $\tau_1 > \tau_2$. τ_1 is used for finding initial edges and τ_2 is used on pixels adjacent to ones already found. For more details on how the Canny Edge detector works see the original paper by Canny from 1986[26]. Once an edge image has been generated, we use the OpenCV command, `Contours` which returns a list of every contiguous group of edge pixels. We denote these contours $\{C_1, C_2 \dots C_M\}$ and each contour contains M_i^c pixels, $C_i = \{p_1^i, p_2^i \dots p_{M_i^c}^i\}$. If the image is not too noisy and we have chosen the threshold values to the edge detection correctly, this should include the particle as a contour.

In order to identify the particle contour a few techniques are used. First, contours whose total size M_c^i is less than some minimum value, n_{min} or larger than some maximum value n_{max} are ignored. Then the average position \mathbf{P}_i of each contour C_i is calculated as the average pixel position

$$\mathbf{P}_i = \sum_{j=1}^n p_j / n$$

which is used to find the distance D_i between each position \mathbf{P}_i and the expected position \mathbf{E} . The expected position is first frame the center of the image and thereafter we assumed the particle have assumed to have constant velocity. So we have

$$D_i = |\mathbf{P}_i - \mathbf{E}|$$

Finally a 'thinness value' for each contour ζ_i is calculated using

$$\zeta_i = \left(\frac{d_{i,max}^2}{M_c^i} \right)^2, \quad (3.4)$$

where $d_{i,max}$ is the longest distance between two pixels in the contour C_i .

Finally a weighted score S_i is assigned to each contour based on its position and thinness using

$$S_i = w_{thin}\zeta_i + \frac{w_{pos}}{D_i} \quad (3.5)$$

where w_{thin} is a weighting constant for the thinness and w_{pos} is a weighting constant for the position.

The contour with the highest score is chosen unless it is lower than some worst acceptable score S_{min}

3.3.4 Adjusting the camera velocity

After two detections of the particle $\mathbf{P}(t_0)$ and $\mathbf{P}(t_1)$, there will have been some change in position which we will refer to as the relative velocity \mathbf{v}_{rel} and the velocity of the step engine as v_{step} and the correctional change in velocity of the step engine \mathbf{v}_{corr} .

If the velocity is larger than some threshold v_{thresh} the step engine velocity is changed by

$$\mathbf{v}_{corr} = \mathbf{v}_{rel}\zeta$$

where $\zeta < 1$ is damping to prevent too sudden changes. If the position of the particle is too far from the center of the image the velocity of the step engine is changed by .

$$|\mathbf{v}_{corr}| = \frac{|\mathbf{P}(t_1)|}{|\mathbf{P}(t_0)|} v_{step}$$

3.4. SUMMARY OF IMPROVEMENTS

where v_ϵ is a small incremental velocity.

3.3.5 Time Considerations

A higher frame rate will allow for greater predictive power and increase stability as the error between frames is reduced. Reducing computational time of each task is important for optimizing the tracking, which also means knowing what tasks are the most demanding. A list of the different tasks and their average execution times can be seen in table 3.1

Task	Average time	Std deviation
Capture screen	41	14
Find edges	78	23
Change velocity	230	62

Table 3.1

We see that the FPS is limited primarily by three routines: The screen capture routine, the change velocity routine and finally the save position routine. The first and last are unavoidable and must be done every frame by definition if we are interested in knowing the particles position as well as possible. This means we simply want to use the velocity correction as little as possible. Since the time constraint is in the communication with the step engine, there is not any optimization to be done here, at least not within the scope of this thesis.

3.4 Summary of improvements

To conclude we return to the problems listed in section 3.2

1. The particles are now all symmetric enough to make useful measurements
2. The particles have low aspect ratios and uniform widths allowing which makes accurate estimations of size possible

3.4. SUMMARY OF IMPROVEMENTS

3. Particles are made from glass meaning they can be trapped using an optical tweezer.
4. The PDMS in the channel is now smooth enough to not be noticed with the microscope.
5. Manual tracking is still necessary when tracking with the optical tweezers.
6. Bubbles are still an issue, but are reduced as one gets more experienced in setting up the experiment.

Part II

Data analysis and results

4

Data Analysis

Once a measurement has been made and a movie recorded the orientational dynamics are estimated. The first step is to identify the particle and approximate it's position and orientation at every point. This is done using software from Johansson [3] and is explained in detail in his thesis and summarized below.

4.1 Particle identification

The first step of the data analysis is to reduce the static noise from the movie caused by dirt, scratches and other defects in the microscope and on the camera lens as can be seen in figure 4.1a. As the noise is static and the actual contents of the image changes the noise is isolated by computing an average frame of all frames in a movie using equation 3.2

An example of such an average frame can be seen in figure 4.1b. The average frame is removed from the camera frame and the result can be seen in figure 4.1c. After this we apply a gaussian smoothing function and Canny edge detection [26] and fill the resulting edge located closest to the previous particle location. The resulting pixels are then fit to an ellipse as described in [3, 27], the ellipse is defined by a length l_e , width w_e and an angle ϕ_p from the x -axis. The filled contour and

the fit ellipse can be seen in figure 4.1d.

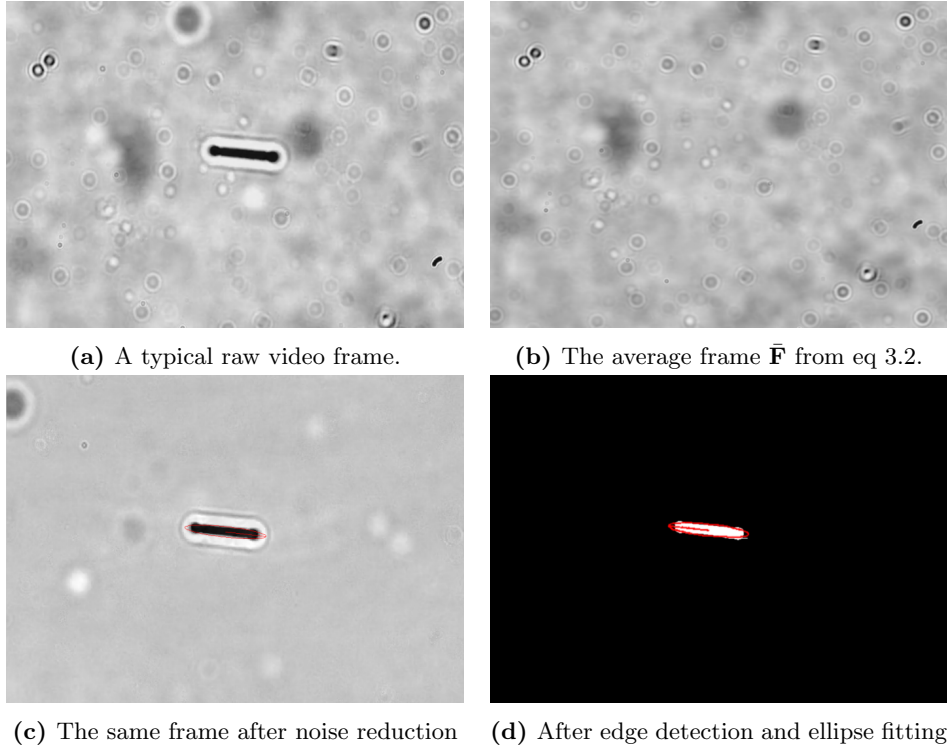


Figure 4.1: These pictures illustrate the most important step of the image analysis from raw image to estimated particle position. First the static noise from the average frame $\bar{\mathbf{F}}$

4.2 Estimation of orientation

The ellipsoid given by the fitting is then our best approximation of the projection in the x - z plane.

The x and z projections of the particle are found by

$$p_x = l_e \sin(\phi_p) \quad (4.1)$$

$$p_z = l_e \cos(\phi_p) \quad (4.2)$$

with x and z projection p_x and p_z .

To find the unit vector \mathbf{n} we need to know the length of the particle. It was shown by Leal

[10] that the particle will always spend a majority of its time aligned with the flow, ie aligned with the camera plane which means that by simply calculating the length L every frame and finding the mode of the distribution we will find a good estimate of L . The particle is normalized by

$$n_x = \frac{p_x}{L}, \quad (4.3a)$$

$$n_z = \frac{p_z}{L}, \quad (4.3b)$$

$$n_y = \sqrt{1 - n_x^2 - n_z^2}. \quad (4.3c)$$

which are the unit vector components used in section 2.3 allowing us to make comparisons between theory and measurement. Until this point the data analysis is the same as that in Johansson [3].

4.3 Width compensation

We have assumed that the particle is a *thin* rod so that the projection \mathbf{p} onto the x and z -axes give us an accurate estimate of \mathbf{n} . However, when we consider that our particle is 'thick' with length l_e as well as width w_e the actual unit vector we will be using in the above algorithms is \mathbf{n}' . The width of the particle will appear as an ellipse even when the particle is aligned completely with the y -axis. Looking at the points when $\phi = 0$, which are the points plotted on the surfaces of section and thus of the most interest, we find

$$\mathbf{n}' = \frac{p'_z}{L} = \frac{p_z \cos(\theta) + D \sin(\theta)}{L} \quad (4.4)$$

which is illustrated in figure 4.2 for 4 different values of θ .

In order to compensate for the width of the particle we modify our projection equation 4.1 to

$$p_x = (l_e - w_e) \cdot \sin(\phi_p) \quad (4.5)$$

$$p_z = (l_e - w_e) \cdot \cos(\phi_p) \quad (4.6)$$

This reduces the particles estimated length by w_e

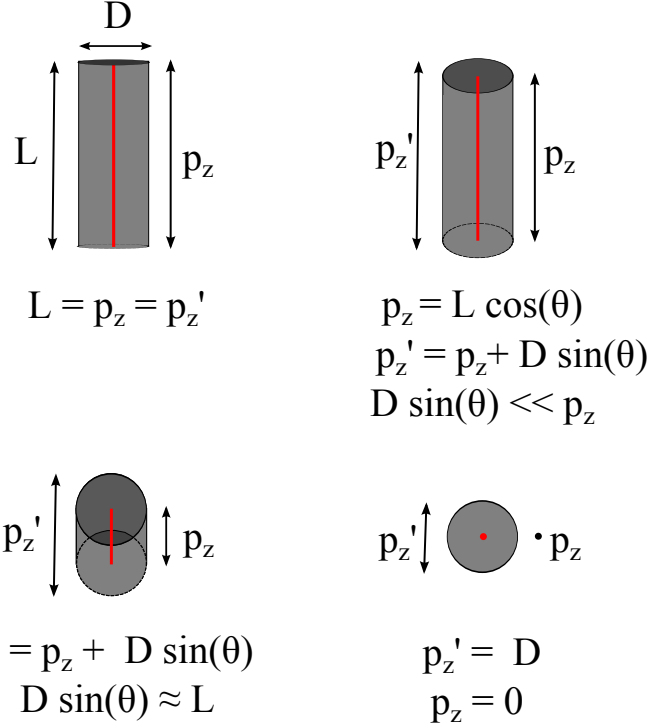


Figure 4.2: Shows the incorrect projection vector p' we obtain from incorrectly assuming the particle is 'thin' in eq. 4.1. The correct projection vector is highlighted in red. Shows four different θ angles at $\phi = 0$.

4.4 Removing tracking errors

The tracking typically contains a few frames where either the view of the particle is visually obstructed or is not detected correctly leading to spikes in the data. To make further theoretical analysis possible the data is corrected by removing such points manually. The basis for removal is

a large discontinuity in the data, and could largely be eliminated with algorithmic means. However in particular for n_z it is very difficult to write an algorithm that will catch all possible edge cases. For example n_z have peaks that make its derivative non continuous which means that cannot be used as a criterion to exclude points. It's thus simpler to look at the analysis program and remove the points where the particle cannot be traced accurately due to noise.

An example of data before and after correction can be seen in figure 4.3 and all uncorrected data files will be available at <http://goo.gl/jgzSXe>.

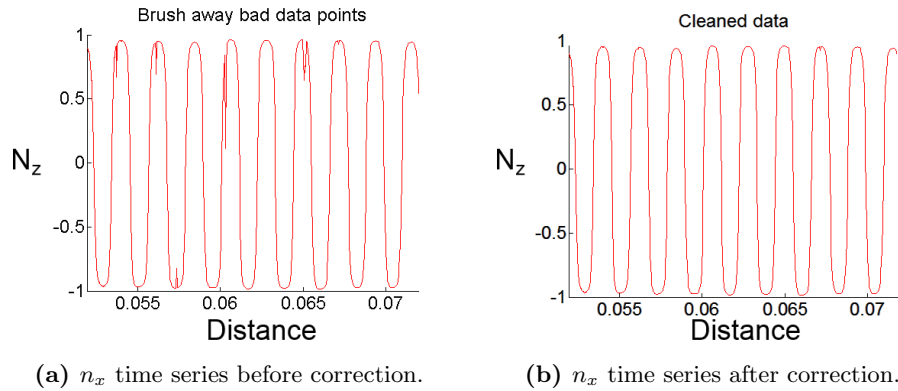


Figure 4.3: Shows a time series of n_x before and after removing points where a significant amount of noise disturbed the tracking.

4.5 Estimating the winding numbers

As discussed in section 2.3.1, estimating the winding number for different types of orientational orbit for one particle allows for a better estimation of ϵ . In order to estimate the winding number for a measured particle we must identify the two periods θ_1 and θ_2 from figure 2.6.

The maxima with the shorter period θ_2 are located where $n_x = 0$ as is seen in figure 4.4. We denote the set of these points P_z . The longer period θ_1 is the periodicity of P_z , marked as red points in Figure 4.4. To estimate the winding number we want to locate the maxima M and minima m in P_z that occur with period θ_1 in the same way we do to find θ_2 in n_z . Unfortunately the height of peaks is noisy and there are few data points for each measurement as the channel is of finite length only allowing a few dozen flips. This means averaging cannot be used to reduce the noise. This

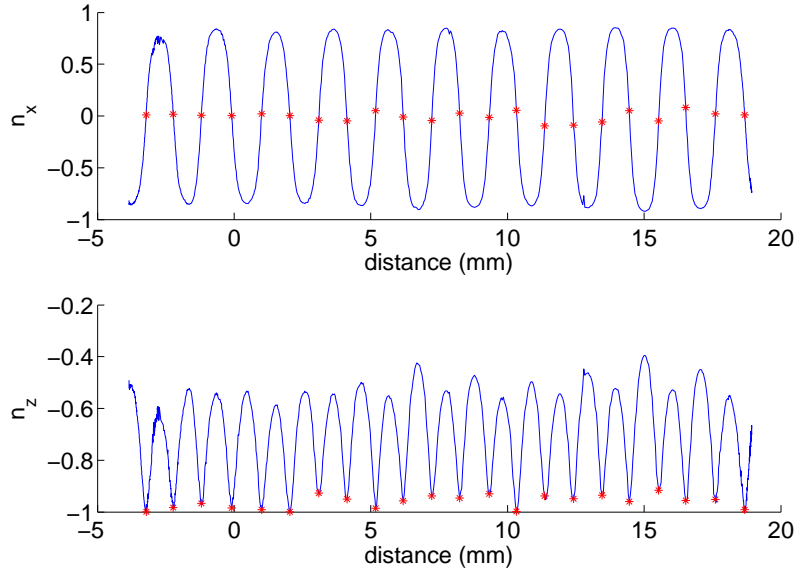


Figure 4.4: The stars are plotted at the same distances in the n_x and n_z plots. We see that zeros of n_x and maxima of n_z occur almost exactly at the same points. These points are referred to as \mathbf{P}_z

means we have no algorithmic means to find θ_1 .

Instead we select from P_z a number of maxima $M_1, M_2 \dots M_p$ and minima m_1, m_2, \dots, m_q . We denote their index in n_z as $I_1^M, I_2^M, \dots, I_p^M$ for the maxima and $I_1^m, I_2^m, \dots, I_q^m$ for the minima. We can then find θ_1 as the mean distance between successive maxima $\overline{d_M}$ and successive minima $\overline{d_m}$,

$$\overline{d_M} = \frac{1}{p-1} \sum_{j=1}^p I_{j+1}^M - I_j^M \quad (4.7)$$

$$\overline{d_m} = \frac{1}{q-1} \sum_{j=1}^q I_{j+1}^m - I_j^m \quad (4.8)$$

$$\hat{\theta}_1 = \frac{\overline{d_M} + \overline{d_m}}{2}. \quad (4.9)$$

In the case that we only have 1 maxima and minima eq. 4.9 can't be calculated so we assume that the distance between a maxima and minima is half a period, i.e.

$$\hat{\theta}_1 = 2 |I_1^M - I_1^m| \quad (4.10)$$

4.6 Matching data to theoretical orbits

To verify that the theoretical Jeffery orbits from 2.3 are present we want to match the measurements to theoretical orbits.

To find the best matching orbit from a Poincaré map for a measurement we again utilize P_z , the points where n_z peaks and $n_x = 0$. We denote the length of \mathbf{P}_z as N . We are concerned with matching them with the peaks from theoretical orbits.

To find the best matching theoretical orbit for a measurement we compute the least square between P_z and all orbits on all phase maps with $\epsilon \in [0.01, 0.02, \dots, 0.1]$ for 200 consecutive different initial ψ (the x -axis on the Poincare map). If we for each orbit denote the theoretical series of n_z peaks as $\mathbf{Q}_z(\theta, \epsilon)$. We let $\mathbf{Q}_z(\theta, \epsilon)$ be of length $M > 2N$ and define $\mathbf{Q}_z(\theta, \epsilon, i)$ to be the n_z series $\mathbf{Q}_z(\theta, \epsilon)$ starting at index i . We assign a score function $S(\theta, \epsilon, i)$ as

$$S(\mathbf{P}, \theta, \epsilon, i) = \frac{1}{N} \left| \mathbf{P}_z - \mathbf{Q}_z^{(i)}(\theta, \epsilon) \right|^2. \quad (4.11)$$

An example experimental P_z series matched to theoretical data is seen in Figure 4.5.

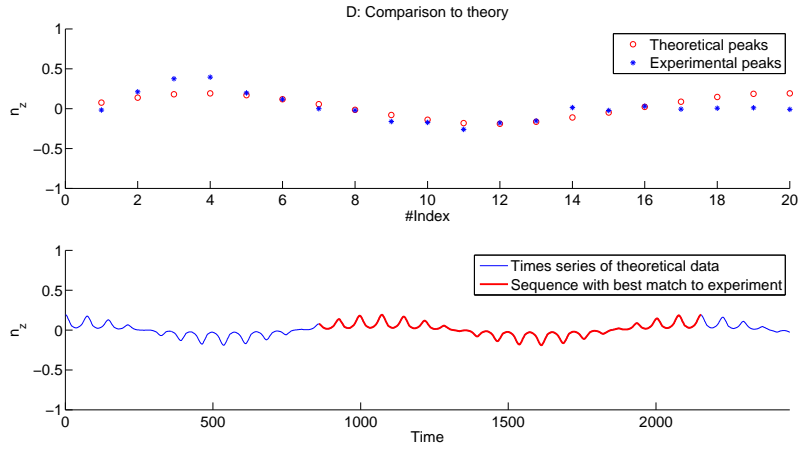


Figure 4.5: The upper figure shows the experimental n_z peaks \mathbf{P}_z versus the theoretical Q_z for the best matching orbit. The lower plot shows where what section of the theoretical time series was used for matching, ie what i from section 4.6 was chosen.

As ϵ will not actually change for a single particle over r different measurements $P_z^{(1)}, P_z^{(2)}, \dots, P_z^{(r)}$, θ and i (the phase) will. So for each ϵ we find the best θ and i using $\hat{S}(\mathbf{P}_j, \epsilon)$

$$\hat{S}(\mathbf{P}_j, \epsilon) = \min(S(\mathbf{P}_j, \theta, \epsilon, i)) \quad (4.12)$$

and then find the best ϵ using

$$\epsilon_{best} = \min\left(\sum_{j=1}^r \hat{S}(\mathbf{P}_j, \epsilon)^2\right). \quad (4.13)$$

It is important to note that this matching has a theoretical limitation. The asymmetry of our cylindrical particles is different from the asymmetry in the triaxial particles used in the theoretical models. The triaxial particles still have a rotational symmetry for rotations of π around any of the major/minor axes. This is not the case with the asymmetric cylindrical particles, which have no rotational symmetry. We therefore have to make the assumption that the difference between these two types of asymmetry is not significant and further theoretical work might reject this assumption.

5

Results

The aim of these measurements is to show that the particles follow the Jeffery orbits and to show that they exhibit quasi-periodic or periodic motion for different initial conditions. In order to show that there are no significant disturbance we examine the reversal. If it reverts perfectly there has been no noise or inertial effects.

During the work of this thesis a large number of movies of particles have been recorded with gradual improvements to the setup primarily in terms of density matching, particle density (the number of particles per liquid volume) and bubble elimination. In this section we present the data from two different particles. These were the only particles where there were good reversals for several stretches for both quasi periodic and periodic orbits. One referred to as particle A, the other as particle B. Particle A is approximately $24 \mu m$ long so it has an aspect ratio $\lambda \approx 8$, particle B is approximately $20.5 \mu m$ long so it has an aspect ratio $\lambda \approx 7$. The measurements in this section were done together with Alexander Laas.

We started each measurement at an approximate depth D and at position $p_0 = (x_0, z_0)$ in the channel relative to the inlet on the right, closer to the pump. We have assumed that the shear is entirely in the y direction when doing our theoretical analysis. This means the flow profile has to be almost entirely flat in the z -direction which it only is if the particle is close to the centre.

Variations do occur but when are less than $10\text{ }\mu\text{m}$ as is seen in figure 5.10.

5.1 Measurements

5.1.1 Measurements of Particle A

Particle A was measured on October 11 in 2013. Two of the measurements made retraced their orbits very well, these are referred to as measurement 1 and measurement 2 which can be seen in Figure 5.1 and Figure 5.1 respectively. Measurement 1 was started with initial condition $n_z \approx 0$ and showed quasi periodic behaviour with a periodic change in amplitude for n_z peaks. Measurement 2 was started with initial condition $n_z \approx 1$ and showed periodic behaviour with very constant n_z peaks.

Other measurement had reversals where the orbit changed considerably, two examples are seen in Figure 5.3 and 5.4. All measurement data for particle A can be found at goo.gl/jgzSXe where particle A is referred to as particle 2 from October 11.

Measurement 1

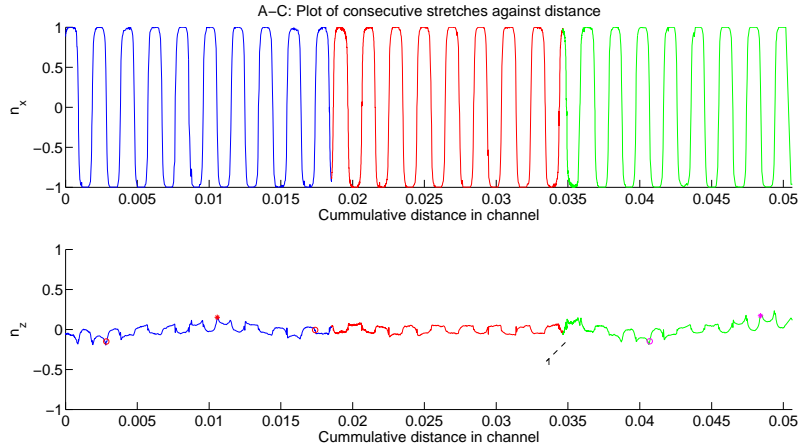


Figure 5.1: The estimate n_x and n_z components of the particle. Despite being very close to a centre orbit there is limited quasi-periodic behaviour as the peaks stay close to 0. The very flattened peaks compared to a low n_z orbit in 2.4b are a result of the width compensation discussed in section 4.3. This particle started $x_0 = 9.8\text{mm}$, $z_0 = 8.9924\mu\text{m}$ and $D \approx 90\mu\text{m}$. This is the same measurement as is used in figure 6.20 in Laas thesis [2]

Measurement 2

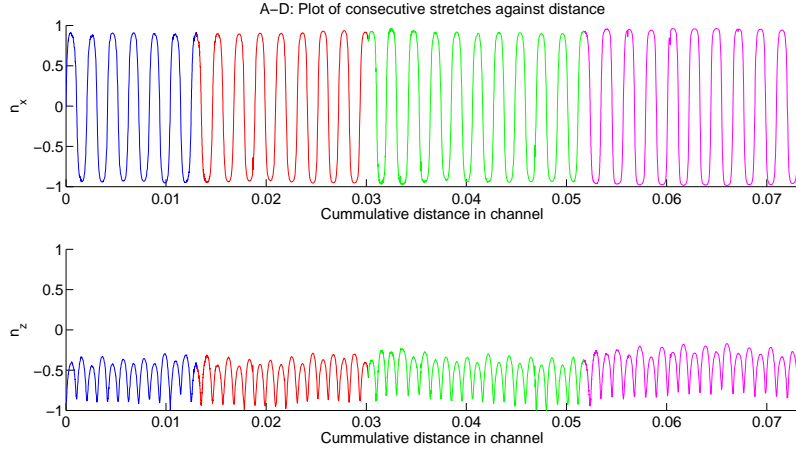


Figure 5.2: The n_z and n_x components for measurement 2 against cumulative distance. The n_z component is consistently close to 1 at the peaks and. The particle started at $x_0 = 26.0\text{mm}$, $z_0 = 275\mu\text{m}$, $D \approx 105\mu\text{m}$. This figure is the same as can be seen in Laas [2] figure 6.21

Measurement 3

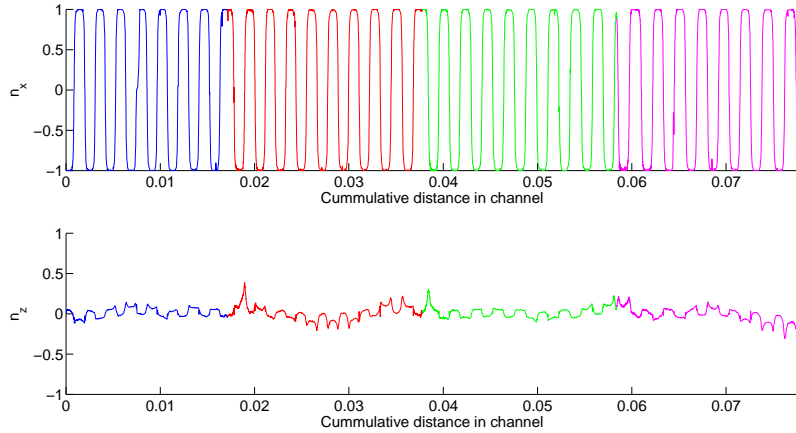


Figure 5.3: The n_z and n_x components for measurement 3 against cumulative distance. The larger peaks that occur after the reversals are not the cause of a tracking error but can be seen clearly in the films. The cause of such a sudden peak and then reverting back to another orbit is not known and we have no good theoretical explanation for it. The reversal of the flow is started when the particle is next to the point marked (3) which is also where there is a change in the orbit. The particle started at $x_0 = 12.3\text{mm}$, $z_0 = 160\mu\text{m}$, $D \approx 100\mu\text{m}$.

Measurement 4

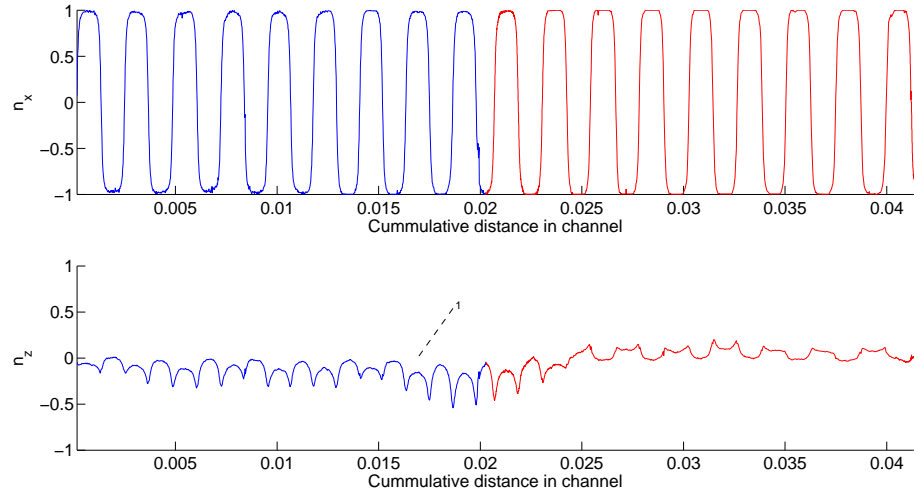


Figure 5.4: The n_z and n_x components for measurement 4 against cumulative distance. The flow is reversed when the particle is at the point marked by (1) and we can see that the peaks around the reversal are larger than for the rest of the measurement. Started at $x_0 = 8.7\text{mm}$, $z_0 = 16\mu\text{m}$, $D \approx 95\mu\text{m}$.

Measurement 5

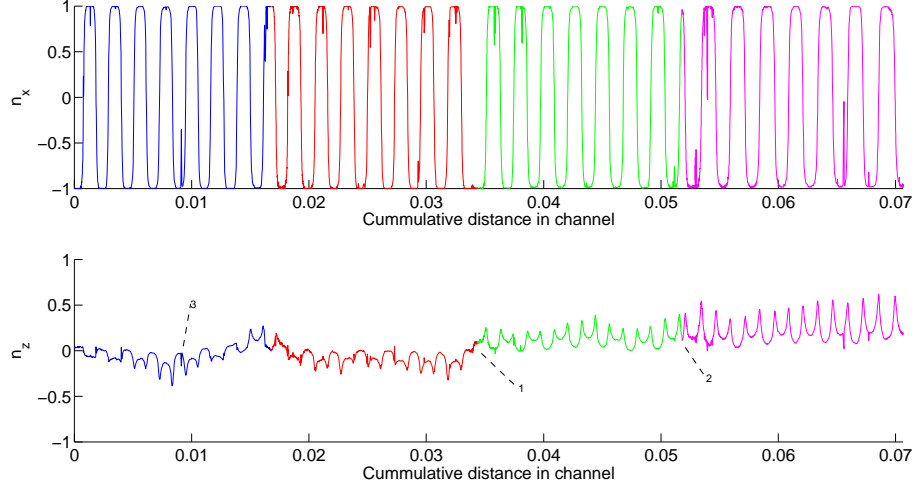


Figure 5.5: The n_z and n_x components for measurement 5 against cumulative distance. At the point marked by (1) n_z changes drastically at the reversal which occurs at the side of the channel closer to the pump. Although there is also some change in the orbit at the reversal marked by (2) it does not move comparably far on the S.O.S. There are a number of small peaks in the data such as the one indicated by (3) which is a consequence is due to insufficient removal of tracking errors, see section 4.4. The particle started at $x_0 = 10.7\text{mm}$, $z_0 = 240\mu\text{m}$, $D \approx 60\mu\text{m}$.

5.1.2 Measurements of Particle B

Particle B was measured on October 1 2013. Particle B has four measurements for which most reversals showed little change in orbit. These are shown below in Figures 5.6, 5.7, 5.8 and 5.9. There were also problematic measurements of particle B analogous to those for particle A, but they have not been included in this section for brevity. All measurement data for particle B can be found at goo.gl/jgzSXe where particle B is referred to as particle 4 from October 1.

Measurement 1

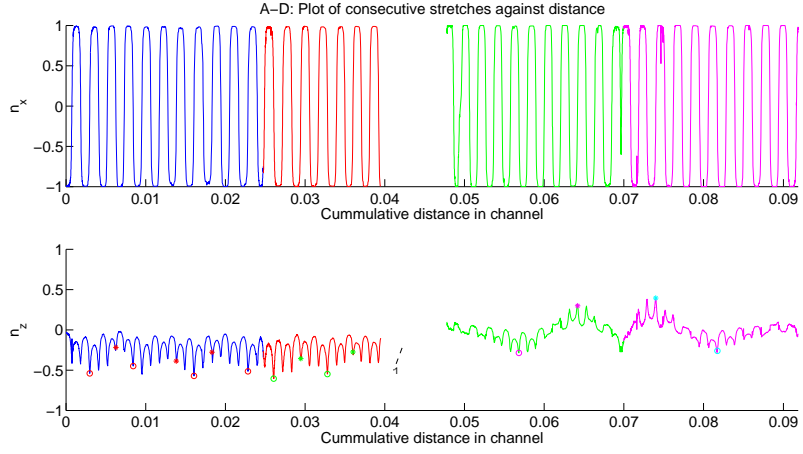


Figure 5.6: The n_z and n_x components for measurement 1 against cumulative distance. The first two and the last two stretches revert very well. In the reversal between the two good reversals there is a large change in orbit which begins at (1) where the flow is starting to revert. This reversal also occurs at the end of the channel closer to the pump. Starts at $x_0 = 9.3\text{mm}$, $z_0 = 35\mu\text{m}$, $D \approx 100\mu\text{m}$. This is the same measurement as is used in figure 6.2 and 6.4 in Laas thesis [2]

5.1. MEASUREMENTS

Measurement 2

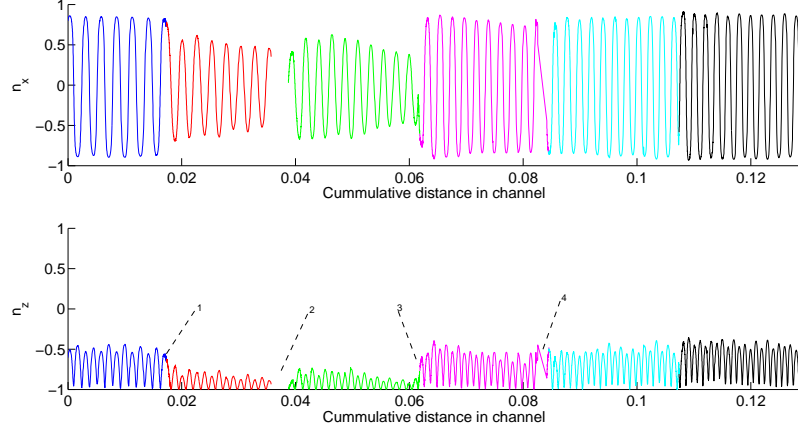


Figure 5.7: The n_z and n_x components for measurement 2 against cumulative distance. The orbit is mostly constant orbit with $n_z \approx 1$ at the peaks. The reversals at (1) and (3) both change the orbit slightly however the difference between the peaks is small and the best matched theoretical orbits in Figure 5.17 are very similar before and after reversals. There is missing data at (2) and (4) where the particle was lost in tracking for some time. The particle started at $x_0 = 28.6\text{mm}$, $z_0 = 72\mu\text{m}$, $D = \approx 85\mu\text{m}$. This is the same measurement as is used in figure 6.8 in Laas thesis [2]

Measurement 3

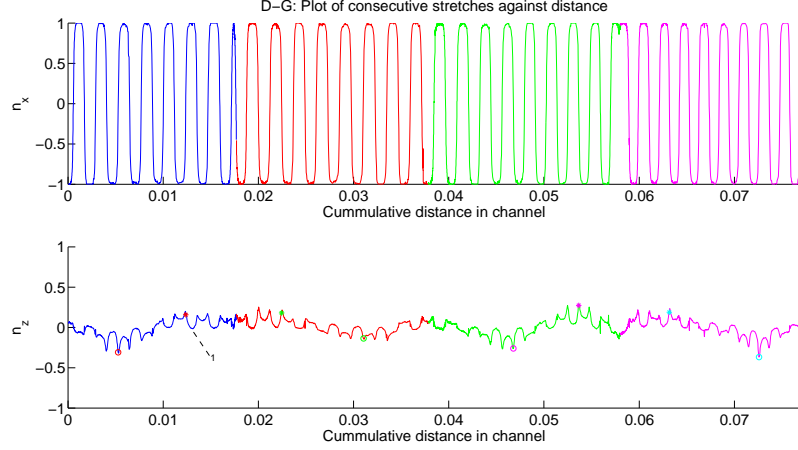


Figure 5.8: The n_z and n_x components for measurement 3 against cumulative distance. The initial condition is $n_z \approx 0$ and the sign changes periodically. Started at $x_0 = 2.7\text{mm}$, $z_0 = 76\mu\text{m}$, $D \approx 90\mu\text{m}$. This is the same measurement as is used in figure 6.10 and 6.12 in Laas thesis [2]

Measurement 4

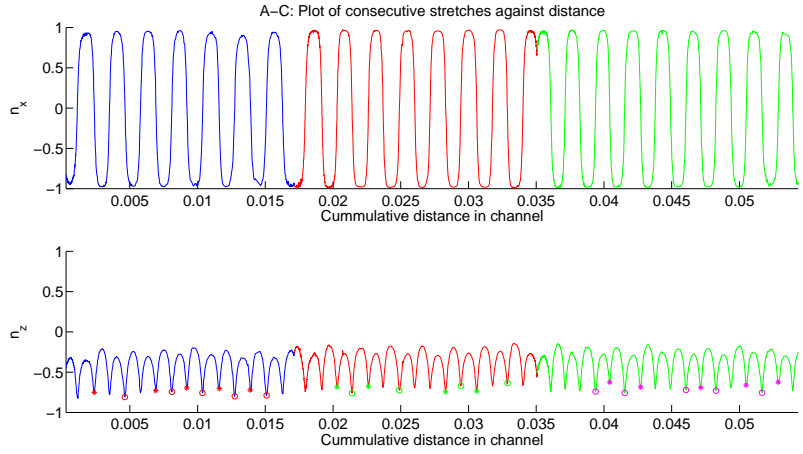


Figure 5.9: The n_z and n_x components for measurement 4 against cumulative distance. While the changes are not large change in n_z there is a periodic variations that could correspond to a sign preserving quasi-periodic orbit. Started at $x_0 = 12.9\text{mm}$, $z_0 = 21\mu\text{m}$, $D \approx 85\mu\text{ m}$

5.2 Diagnostic plots

A number of diagnostic measurements were made for each particle to find possible problems with the setup. In this section we only show the diagnostic measurements from measurement 1 for particle A, and from measurement 2 for particle B but all diagnostic plots can be found at <http://goo.gl/jgzSXe>.

5.2. DIAGNOSTIC PLOTS

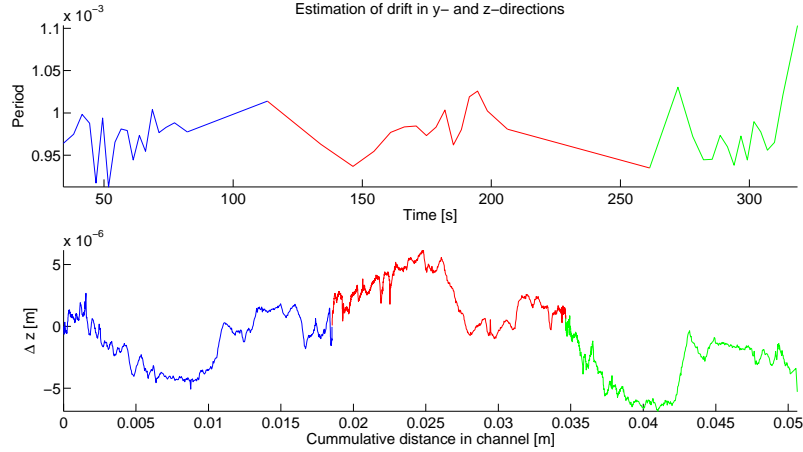


Figure 5.10: The estimation of drift in y and z direction for Particle from measurement 1. Upper figure is the estimation of the sinking of the particle, the lower figure is the measured z position in the channel against cumulative distance.

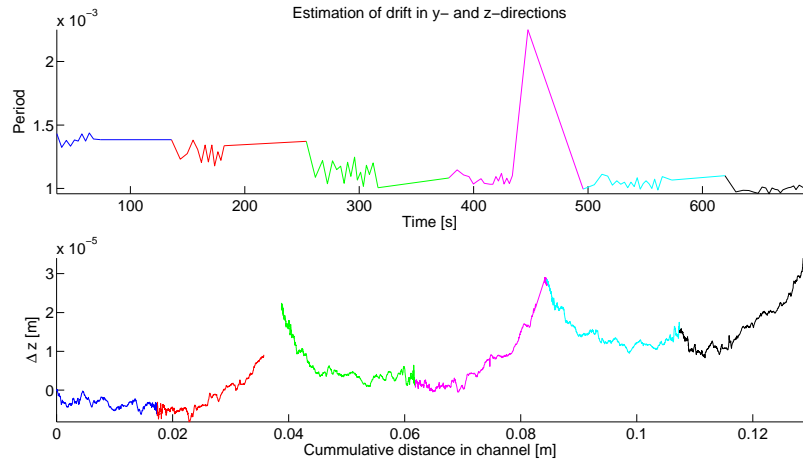


Figure 5.11: The estimation of drift in y and z direction for Particle from measurement 1. Upper figure is the estimation of the sinking of the particle, the lower figure is the measured z position in the channel against cumulative distance.

The center of mass movement in the direction perpendicular to the flow direction x is seen in Figures 5.10 and 5.11. Movement in the y direction, i.e. sinking or floating, was measured by plotting the period of each flip against time as in the upper graph of figure The period here refers to the distance Δ_i between two successive zeros for n_x relative to the first such distance Δ_0 . If

5.2. DIAGNOSTIC PLOTS

there is no clear trend to higher or lower values it implies that there is little sinking or floating.

The movement in the z coordinate is very small relative to the movements in the x direction. We can see that Z-direction movements along one stretch are on the order of $10\mu m$ compared to the x direction which is on the order of $2 \cdot 10^4 \mu m$. The change in period was less than 20% for all particles presented in this chapter.

The speed was plotted as a function of time to see how the flow reversed and if there were any problems with the pump. There is a noticeable difference between reversals that occur on the side of the channel and the side closer to the pump where on the reversal on the end of the channel further from the pump the speed drops to 0, increases for a short while and then goes back down to 0. This has been a consistent feature across all measurements.

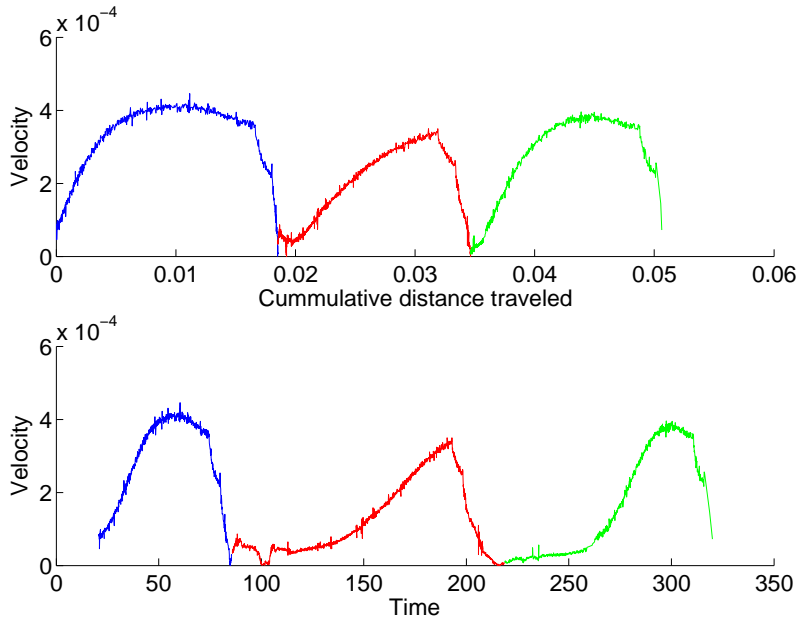


Figure 5.12: The speed (note not the velocity) of the particle A from measurement 1 against cumulative distance in the upper figure and against time in the lower figure.

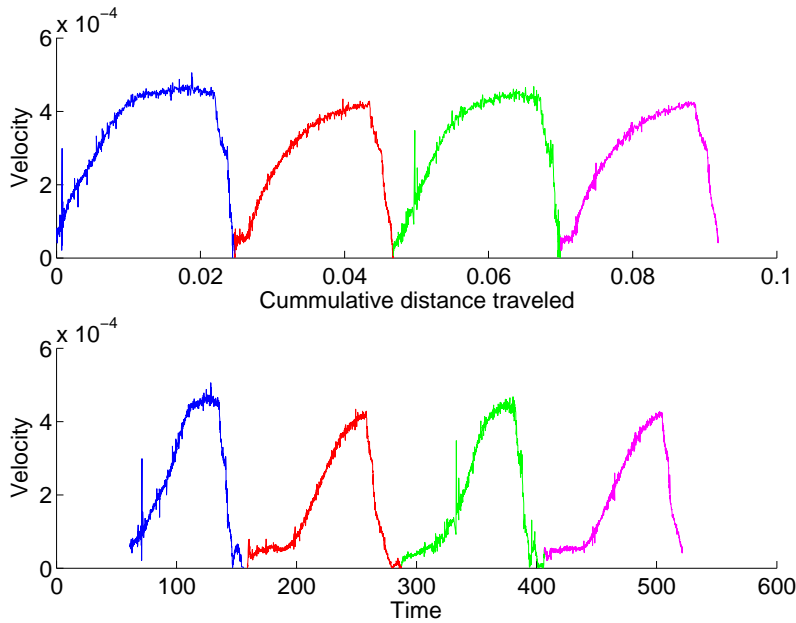


Figure 5.13: The speed (note not the velocity) of particle B from measurement 2 against distance in the upper figure and against time in the lower figure. In the plot against time there is an extra dip to 0 at around $t = 150$ and $t = 400$. This occurs at the end of channel further away from the pump.

5.2.1 Reversals

In order to show that the dynamics of the particle revert when the flow is reversed we plot the components of \mathbf{n} against distance in the channel. The first reversal from measurement 1 for particle A is seen in Figure 5.14. There is very good agreement along the entire length of the channel only at the very end does there a difference larger than the margin of error. The same plot is made from the second reversal from measurement 5 in Figure 5.15. Here the particle changes orbit drastically at the reversal while being stable before and after.

5.2. DIAGNOSTIC PLOTS

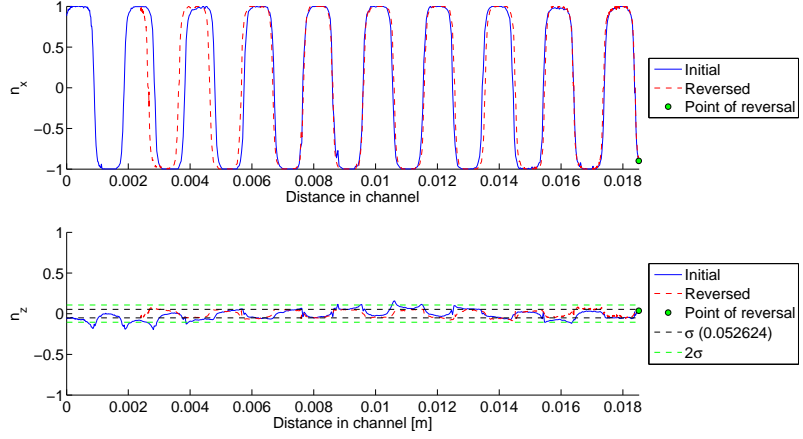


Figure 5.14: Shows n_x and n_z first and second stretches from Measurement 1, seen in figure 5.1 but against the actual position in the channel as opposed to cumulative distance. There is an almost perfect match along the entire channel for n_x and only small disagreement for n_z . The dashed lines indicate the error margins for detecting $n_z = 0$. This figure is the same as can be seen in Laas[2] figure 6.21

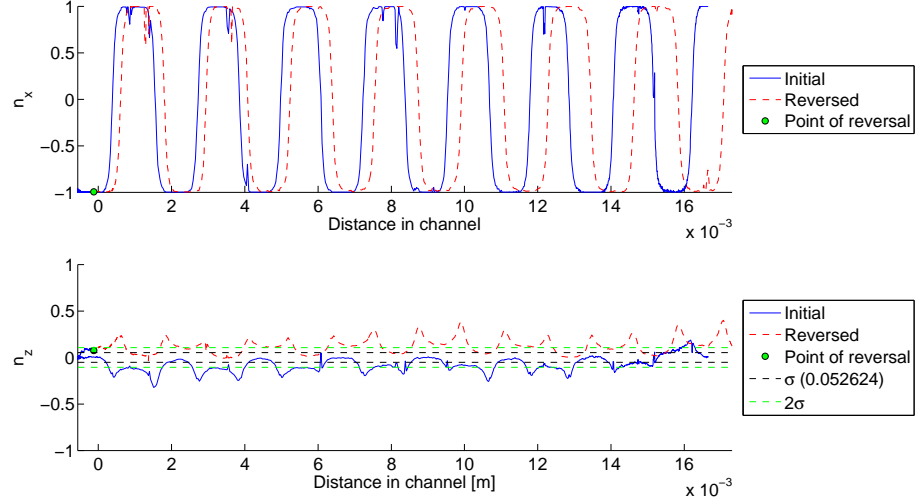


Figure 5.15: n_x and n_z from figure 5.5 for the second and third stretch plotted against actual distance instead of commutative distance. The reversal occurs at the left and although there is some moderate agreement in n_x the match in n_z is non existant from the very start.

5.3 Match to theoretical orbits

5.3.1 Particle A

Particle A is approximately $24 \mu m$ long so it has a λ close to 8 and the closest match for the asymmetry is $\epsilon = 0.02$. 5.1

Using the algorithm described in section 4.6 we match the data from measurement 1 and 2 for particle A to find the closest matching ϵ and the best matching orbits. This is shown in Figure 5.16. We can see that particle A is in a quasi-periodic circular orbit during measurement 1, it is matched to the lines indicating A B and C for the first, second and third stretches respectively. After being shifted by the optical tweezer particle A followed a periodic orbit during measurement 2. Measurement 2 is matched to the orbids D, E, F and G for the first, second, third and fourth stretches respectively.

5.3. MATCH TO THEORETICAL ORBITS

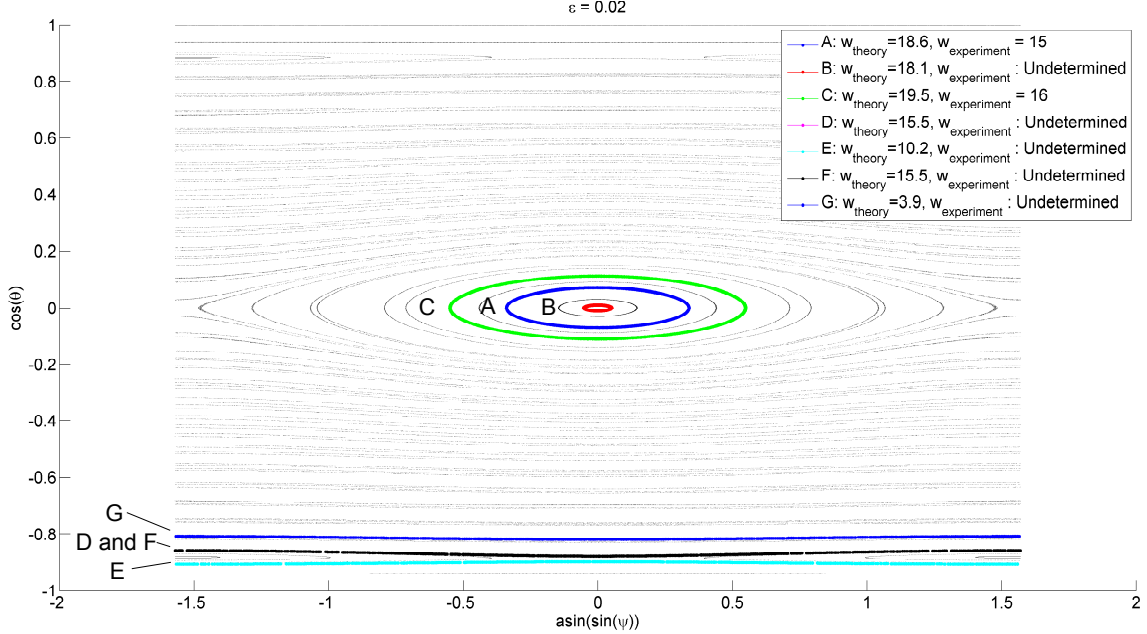


Figure 5.16: Gray lines represent the phase map for $\lambda = 8$ and $\epsilon = 0.02$. The measured λ was 8.2 ± 0.1 . The orbits of the best fit theoretical fits to measurements are highlighted stretch by stretch. None of the orbits for this particle had any large variation despite being very close to $n_z = 0$. The winding numbers are within 50% of the estimates but both are too low, suggesting that the ϵ might be too low.

5.3.2 Particle B

The same procedure is repeated for particle B using the data from measurement 1,2, 3 and 4. To make the graph less cluttered it is split into two figures, Figure 5.17 for measurement 1 and 2 and Figure 5.18 for measurement 3 and 4. We can see that particle B is in a quasi-periodic circular orbit , it is matched to the lines indicating A B and C for the first, second and third stretches respectively. After being shifted by the optical tweezer particle A followed a periodic orbit during measurement 2. Measurement 2 is matched to the orbits D, E, F and G for the first, second, third and fourth stretches respectively.

5.3. MATCH TO THEORETICAL ORBITS

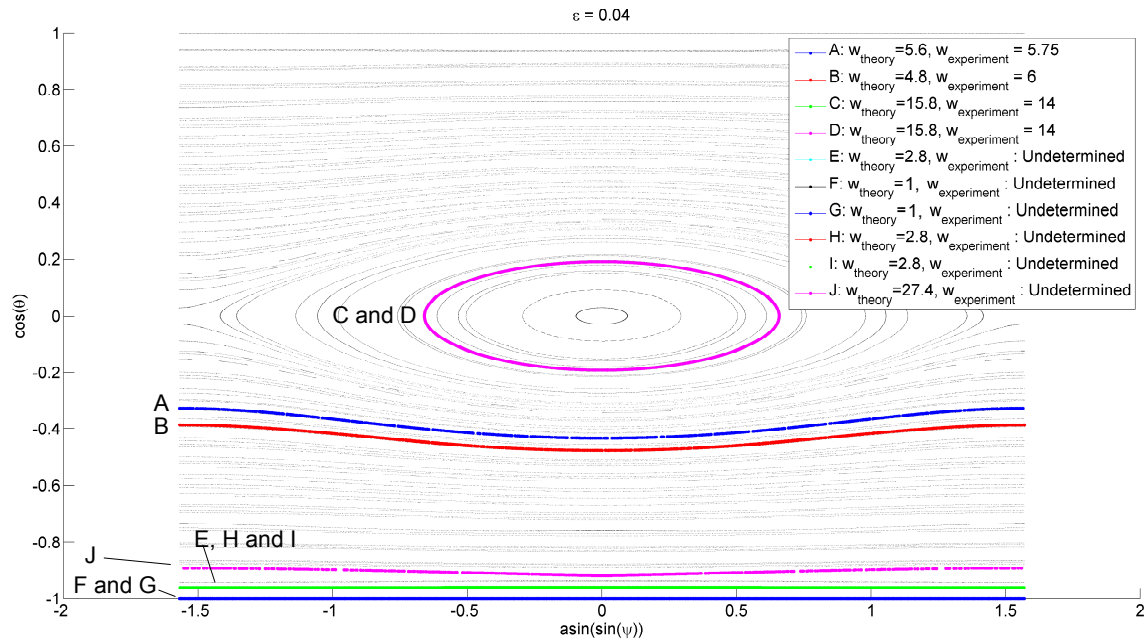


Figure 5.17: Grey lines represent the poincaré map for $\lambda = 7$ and $\epsilon = 0.04$, the estimate of λ from measurement was 6.7 ± 0.1 . The highlighted orbits are the best fits to the stretches from measurements 1 and 2, A-D from measurement 1 and E-I from measurement 2.

5.3. MATCH TO THEORETICAL ORBITS

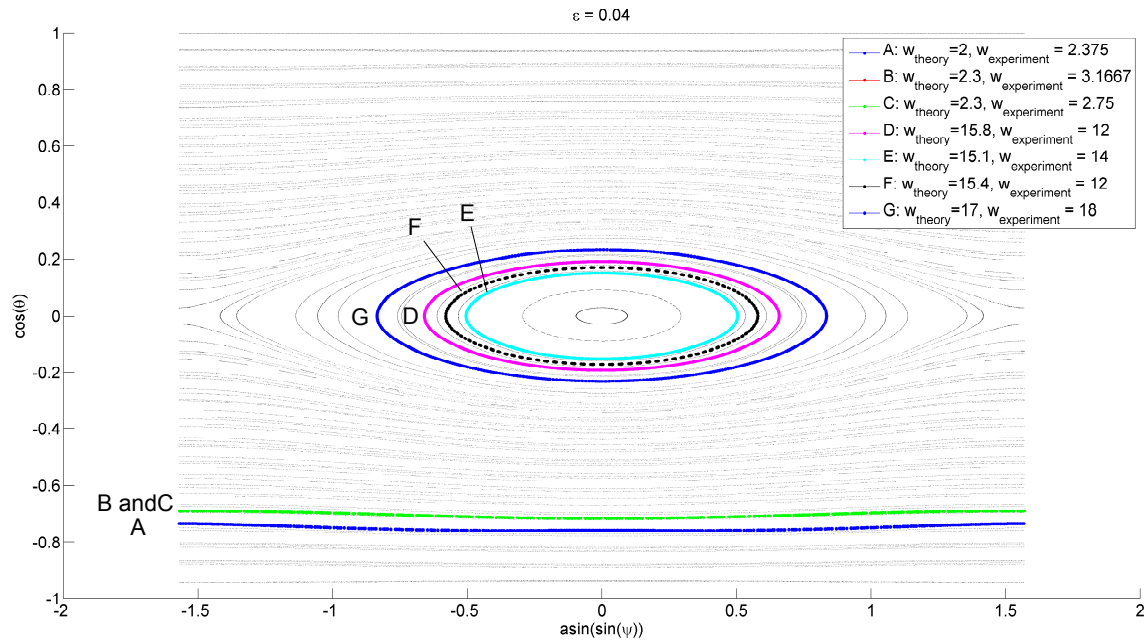


Figure 5.18: Gray lines represent the poincaré map for $\lambda = 7$ and $\epsilon = 0.04$. the estimate of λ from measurement was 6.7 ± 0.1 . The highlighted orbits are the best fits to the stretches from measurements 3 and 4.

6

Discussion

The primary goal of this thesis is to experimentally verify that asymmetric particles in shear flow will exhibit different types of motion for different initial conditions as was shown by Yarin *et al* [11]. To verify that there was no significant amount of noise we look at the reversal of the flow and if the particle retraces its motion it confirms a lack of noise as well as a lack of inertial effects. To estimate the asymmetry ϵ of the particles we try to match the experimental trajectories over several of several measurements with theoretical orbits. We also utilize the winding number of quasi-periodic orbits where we can detect it to confirm that the match is valid.

Looking at figures 5.18, 5.17 and 5.16 we find both quasi-periodic and periodic motion as well as all three types of orbits discussed in section 2.3.1. The winding numbers for the orbits where we can measure it are within 50% of our theoretical predictions. This suggests that we have observed both quasi-periodic orbits and periodic orbits for the same particle two times. We do however have to consider the assumption we make regarding the symmetry difference between the damaged cylinders used experimentally and the flattened spheroids use in theoretical models.

This is however the results from a few measurements of two particles, there are many other measurements that have reversals where there are large differences before and after such as in Figure 5.15 and Figure 5.5. There are four major problems in the data

1. Sinking
2. Bad reversals
3. Too few flips to clearly estimate winding number
4. Unexplained changes in orbit

6.1 Sinking

One of the major problems with this setup compared to the previous setup used by Einarsson *et al* [1] is matching the density of the fluid to that of the particles. Even small mismatch of 0.05 g/ml we find using eq. (2.5) a sinking speed of $= 4.9 \cdot 10^3 \mu\text{m}/\text{s}$. In earlier measurements the pump speed was $3 \mu\text{l}/\text{minute}$ and the particle were 60% larger, which meant the sinking occurred more than twice as long and twice as fast which meant it was a larger problem. Even now though it can be noticeably as in longer measurements such as in figures 5.7 and 5.11.

6.2 Reversals

Almost every measurement with several stretches have a reversal where the particle noticeably changes orbit. This can been seen in Figures 5.5, 5.4 and 5.6. While there is a trend that bad reversals occur at he end further from the pump, there are many exceptions to this. There are many cases where the orbit begins to change just as the flow is starting to reverse, such as in figure 5.4. The particle Reynolds number depends on the velocity relative to the particle so a possible culprit would then be that reversals occur too rapidly and increase the Re_p such that the $Re_p \ll 1$ condition from Jeffery [8] does not hold. We have not been able to draw any clear conclusion and solving issues with reversals would be a tremendous improvement.

6.2.1 The speed of the particle

A possible cause of bad reversals are too rapid reversals and to prevent this the reversals are incremental as discussed in Section 3.1.

Possibly increasing this staggering on the first part might make a difference, but if we look at the speed of the particle A in Figure 5.12 and particle B in Figure 5.13 we see that after a rather sharp decline in speed the acceleration is very slow. Almost all of this acceleration occurs while the pump is infusing or withdrawing at a fixed rate. The liquid in the channel accelerating while the pump rate constant implies that there is a noticeably expansion in the channel. To verify this we look again at Figures 5.12 and 5.13.

If we have an expanded/contracted channel it should have different effects on different sides of the channel. We expect that when we revert the flow with the particle on the side closer to the pump the channel will have a small impact and the flow would revert quickly. However when we the flow is reversed and the particle is on the far end of the channel we should have an impact. The 'extra' fluid that is in the expanded channel would be withdrawn before any pressure is felt on the far side. This would cause a delay where there is no acceleration for some time while after the pump reversed.

This behaviour is exactly what we see in all speed plots like 5.12 and 5.13. For reversals on the far end of the channel there is a second dip where the particle goes to $|v| = 0$. On the end closer to the pump this never occurs.

An earlier theory for the delay would be an offset in the pump, for example a distance between the syringe handle and the pump holder which would need to be traversed, but this would occur at both ends of the channel and would not explain the very long acceleration of the fluid.

How this impacts the dynamics is not clear, most bad reversals occur at the end of the channel close to the pump, which suggests that this extra elasticity in the system might in fact be positive.

6.3 Winding number matching

Using the score function \hat{S} as described in section 4.6 to find the closest matching orbit is useful, it only gives the best fit. Instead we use the winding number to validate or dismiss a matched orbit and an estimated ϵ . The winding number can only be used for the orbits where n_z changes noticeably, i.e. the quasi-periodic orbits, but these are also the ones of primary interest. If we look at figure 2.7 we see that the difference in winding number of the same θ is on the order of a factor 2 between $\epsilon = 0.01$ and $\epsilon = 0.05$ for circular orbits, and still quite noticeably different between $\epsilon = 0.05$ and $\epsilon = 0.10$. However the largest difference is where the change from circular to bent orbit occurs.

When we look instead at orbits for large $|n_z|$ such as in Figure 5.17 or for $n_z \approx \psi \approx 0$ such as orbit B in figure 5.16 the orbits for different ϵ, λ and i are all largely the same. The differences in n_z are too small for us to reliably detect. This creates a problem for detecting particles with very small ϵ . For n_z that are very small, we cannot distinguish the orbits for a small ϵ particle with higher ψ orbit for a high ϵ particle with a low ψ orbit. For higher n_z we cannot distinguish straight lines from straight lines. And in the intermediary we are unable to detect a $w > 20$, at best finding a sloping n_z which might just be undesired reversals. Particle A has several orbits that are matched in the intermediary circular n_z region which we can distinguish from $\epsilon = 0$ but we can not estimate the winding number especially well as we barely have a half period.

6.4 Unexplained behaviours

In a number of measurements there are changes in orbit for which we have no good explanation. For example in figure 5.5 the second reversal is completely sharp, the orbit virtually instantly changes, completely 'forgetting' the previous orbit. Why does this occur with the same particle, the same setup, that produce the excellent reversals in figure 5.1. In everything we can control all conditions are the same. The only difference is the z coordinate, yet figure 5.3 was measured at a similar z and showed very few odd behaviours.

6.5 Width compensation

The width compensation discussed in Section 4.3 does solve the issues the previous algorithm had with 'thick' particles for n_z close to 0. It does still produce small errors for $n_z \neq 0$. However it was discovered that Eq 4.4 can be solved explicitly. Given the actual length L of the particle the Euler angle θ can be solved for at each point after a measurement is complete. This would improve the resolution of peaks and allow for more accurate results.

6.6 Goodness of fit

The method for matching the data to a theoretical orbit described in 4.6 finds the best fit but it is important to know how good of a fit. A flat fitness curve would mean a very small change in the data could lead to a very large change in our matched orbit. To determine the goodness of fit we vary the three parameters separately and find the best fit for the other two parameters. In Figure 6.1 we find the best matching orbits for Particle A for asymmetries ranging from 0 to 0.2. We see that there is a clear minima around $\epsilon = 0.02$ implying that it is a good fit.

In Figure 6.2 the match of stretch 1 from measurement 1 of particle A is matched. We use the best matching asymmetry, match for orbits from the center of the pointcare map to the top. For each orbit we find the best starting position (the initial ψ). The result is a steady slope down to the correct orbit suggesting that this variable also had a clear best value that was chosen.

The best In Figure 6.3 we use the best matching asymmetry and orbit for stretch 1 from measurement 1 of particle A, and the starting position (initial ψ) is varied over 1 full period. The relatively flat slope suggests that this parameter while certainly improving the fit slightly is not as important as the other two parameters.

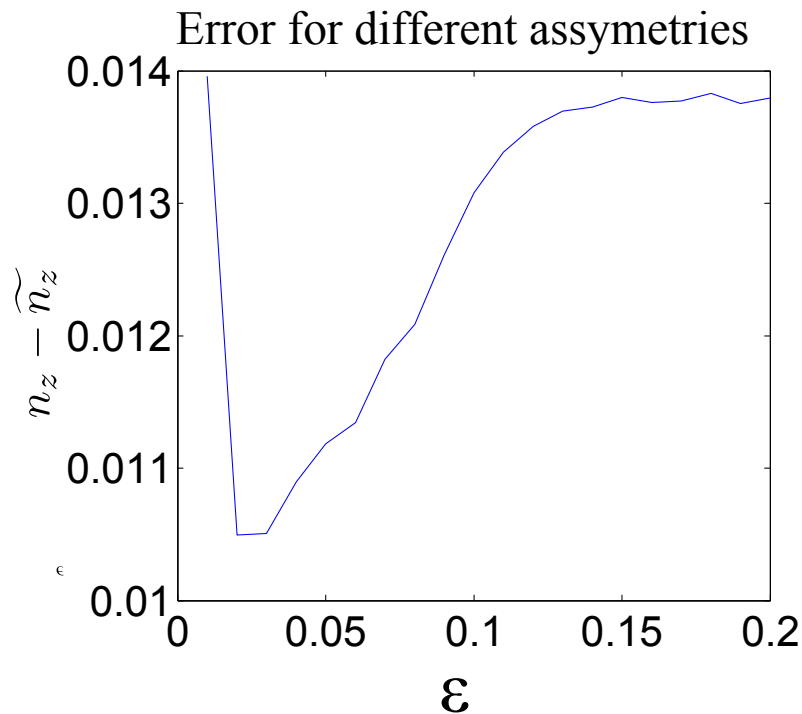


Figure 6.1: We see how the difference between the theoretical n_z and all the measured \widetilde{n}_z for all measurements of particle A for different asymmetries ϵ . For each asymmetry we find the orbit and the initial ψ with the smallest distance for each stretch. We see that there is a clear minima around $\epsilon = 0.02$

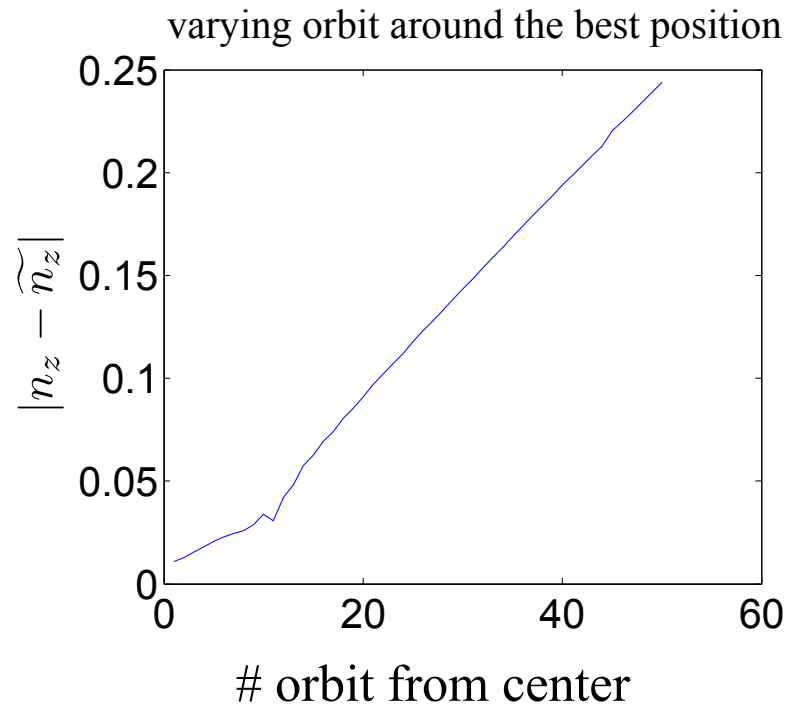


Figure 6.2: The difference between the theoretical n_z and the measured $\widetilde{n_z}$ for the first stretch of the measurement 1 for particle A (seen in figure 5.1) with the best asymmetry for different orbits. .

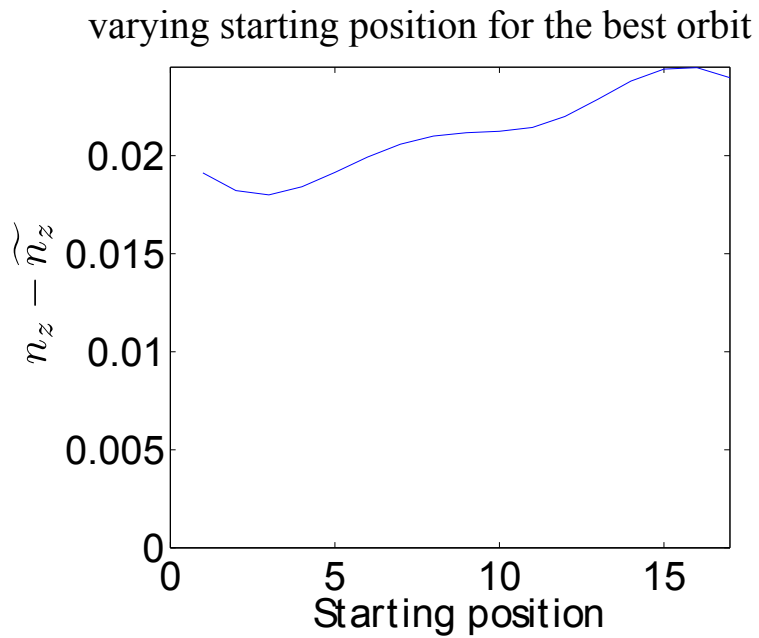


Figure 6.3: The difference between the theoretical n_z and the measured \widetilde{n}_z for the first stretch of the first measurement for particle A. The best orbit and best asymmetry are chosen, but different initial conditions are tested.

7

Conclusion

the Jeffery Orbits are frequently used across scientific fields but thus far there has been few experimental studies of the orientational dynamics and in particular the quasi-periodic and chaotic orbits have only been studied experimentally by Einarsson *et al*[1][24]. The goal of the thesis was to verify the theoretical predictions of Yarin, Hinch and Leal [10, 11] and to show that the same particle could exhibit quasi periodic and periodic behaviour for different initial conditions.

There are several measurements that agree very well with theoretical models using both the phase map matching the winding number estimation. Further more different initial conditions exhibit very different behaviours across different particles, either being almost constant to being quasi-periodic with a large regular variation. We can then conclude to have managed to measure the orbits predicted by Yarin, Hinch and Leal [10, 11].

The time reversibility is unreliable, for some measurements the dynamics revert very well, and for others does not. We have not understood well what causes this type of unpredictability that can occur for the same particle only minutes apart. The primary focus of future efforts should go into understanding and correcting whatever issues causes the reversals to be so unreliable. It is possible that time reversal can be improved by attempting to somehow increasing the viscosity without changing the optical index of the liquid or by slowing down reversals. Another possibility

is limiting the significant expansion and contraction of the channel that seems to occur.

The automated tracking was useful, but with the increased speed of measurements as well as smaller particles there needs to be a better predictive model to not lose the particle in reversals. It is also less needed as measurements take significantly less time, but if significantly slower reversals are the preferred way of improving time reversibility then it could be more relevant.

Bibliography

- [1] J. Einarsson, et al., Periodic and aperiodic tumbling of microrods advected in a microchannel flow, *Acta Mechanica* (2013) 1–9.
- [2] A. Laas, A study of periodic and quasi-periodic motion of microrods in a shear flow using optical tweezers, Msc thesis, Chalmers University of Technology.
- [3] A. Johansson, Analysis of empirical data on the tumbling of microrods in a shear flow, Master's thesis, Chalmers Univeristy of Technology (2012).
- [4] J. Einarsson, Low reynolds number particle dynamics, Master's thesis, Chalmers Univeristy of Technology.
- [5] T. Kaya, H. Koser, Characterization of hydrodynamic surface interactions of escherichia coli cell bodies in shear flow, *Phys. Rev. Lett.* 103 (2009) 138103.
- [6] E. Cañón-Tapia, M. Chávez-Álvarez, Rotation of uniaxial ellipsoidal particles during simple shear revisited: the influence of elongation ratio, initial distribution of a multiparticle system and amount of shear in the acquisition of a stable orientation, *Journal of Structural Geology* 26 (11) (2004) 2073 – 2087.
URL <http://www.sciencedirect.com/science/article/pii/S0191814104000690>
- [7] A. Einstein, A new determination of molecular dimensions, *Annalen der Physik*.

BIBLIOGRAPHY

- [8] G. B. Jeffery, The motion of ellipsoidal particles immersed in a viscous fluid, Proceedings of the Royal Society A 102.
- [9] P. J. Gierszewski, C. E. Chaffey, Rotation of an isolated triaxial ellipsoid suspended in slow viscous flow, Canadian Journal of Physics 56 (1) (1978) 6–11.
- [10] E. J. Hinch, L. G. Leal, Rotation of small non-axissymmetrical particles in a simple shear flow, J. Fluid Mech 92 (1979) 591–608.
- [11] A. L. Yarin, O. Gottlieb, I. V. Roisman, Chaotic rotation of triaxial ellipsoids in simple shear flow, J. Fluid Mech vol 340 (1997) 83–100.
- [12] F. C. van den Bosch, lecture 1: Surfaces of section, Online material for course.
- [13] H. L. Goldsmith, S. G. Mason, The flow of suspensions through tubes i. single spheres, rods, and discs, Jounrla of colloid science (17).
- [14] O. Harlen, D. Koch, Orientational drift of a fibre suspended in a dilute polymer solution during oscillatory shear flow, J. Non-Newtonian Fluid Mech. 73 (1997) 81–93.
- [15] C. J. S. Petrie, The rheology of fiber suspensions, J. of non-newtonian fluid mechanics 87.
- [16] J. Einarsson, Orientational dynamics of small non-spherical particles in fluid flows, Licentiate thesis, Gothenburg University (2013).
- [17] T. Pedley, Introduction to Fluid Dynamics, Department of Applied Mathematics and Theoretical Physics, University of Cambridge, Silver St., Cambridge CB3 9EW, U.K., 1997.
- [18] S. Childress, An Introduction to Theoretical Fluid Dynamics, Cambridge University Press, 2008, page 117 Starts the discussion of time reversibility of Stokes' Flow.
URL www.math.nyu.edu/faculty/childres/fluidsbook.pdf
- [19] G. K. Bachelor, An Introduction to Fluid Dynamics, Cambridge University Press, 1967, page 212 is definition of Reynolds Number, page 233 is Stokes Law.
- [20] J. Diebel, Representing attitude: Euler angles, unit quaternions, and rotation vectors (2006).

BIBLIOGRAPHY

- [21] J. Munkhammar, Poincare map (2013).
URL mathworld.wolfram.com/PoincareMap.html
- [22] B. L. at Stanford, Optical tweezers an introduction.
URL www.stanford.edu/group/blocklab/Optical%20Tweezers%20Introduction.htm
- [23] Fabrication of PDMS microfluidic channels (2010).
URL cismm.cs.unc.edu/wp-content/uploads/2011/03/MicrofluidicsLab.2010.pdf
- [24] Y. N. Mishra, J. Einarsson, et al., A microfluidic device for studies of the orientational dynamics of microrods, Proc. SPIE 8251 2825109.
- [25] Nippon Electrical Glass Co, Gap spacers for LCDs: Microrods, www.neg.co.jp/epd/elm/e_prd/other/others_01.pdf.
- [26] J. Canny, A computational approach to edge detection, Pattern Analysis and Machine Intelligence, IEEE Transactions on PAMI-8 (6) (1986) 679–698.
- [27] S. N. Wijewickrema, A. P. Paplinski, C. E. Esson, Reconstruction of spheres using occluding contours from stereo images, in: Pattern Recognition, 2006. ICPR 2006. 18th International Conference on, Vol. 1, IEEE, 2006, pp. 151–154.